Charge Carrier Dynamics in Perovskites

von

Christopher Gort

Masterarbeit in Physik
vorgelegt dem Fachbereich Physik, Mathematik und Informatik (FB 08)
der Johannes Gutenberg-Universität Mainz
am 26.02.2019

1. Gutachter: Prof. Dr. Stefan Weber
2. Gutachter: Prof. Dr. Hans-Joachim Elmers

Ich versichere, dass ich die Arbeit selbstständig verfasst und keine anderen als die angegebenen Quellen und Hilfsmittel benutzt sowie Zitate kenntlich gemacht habe.

Mainz, den 26.02.2019[Unterschrift]

Christopher Gort
Institut für Physik
Staudingerweg 7
Johannes Gutenberg-Universität D-55099 Mainz
cgort@students.uni-mainz.de

"Be best"
-Melania Trump

Table of contents

Zusammenfassung

Perowskit Solarzellen sind eine neuartige Gattung der Solarzellen, welche innerhalb kürzester Zeit eine rasante Entwicklung zeigten. Dabei fand man exotische Effekte, wie eine J-V Hysterese, welche andere Solarzellen nicht zeigen. Es herrscht Konsens unter Wissenschaftlern, dass diese J-V Hysterese durch Ionenbewegung innerhalb des Perowskitabsorber bedingt ist, welche auf Millisekunden Zeitskalen stattfinden

Um mögliche Ladungsträgerbewegungen lokal und zeitlich aufzulösen eignet sich die Methode der Kelvin-Sondenmikroskopie (KPFM). Im ersten Teil dieser Arbeit untersuchen wir die zeitliche Auflösung unseres KPFM Aufbaus und stellen heraus welche Zeitskalen innerhalb unserer zeitlichen Auflösung liegen.

Um KPFM auf Solarzellen zu messen benötigt man einen nanometer-flachen Querschnitt der Solarzelle. Basierend auf einer Poliermethode von Weber et al.[1], entwickeln und charakterisieren wir im zeiten Teil eine neuartige Methode, welche ein Hitachi IM4000 Poliergerät nutzt, um schnell große Flächen solcher Querschnitte zu präparieren.

Im dritten Teil testen wir diese Methode vergleichend an einer mesoporösen und einer planar Perowskit Solarzellearchitektur. Diese beiden Architekturen zeigen unterschiedliche Grade der J-V Hysterese. In unserem Vergleich untersuchen wir die Dynamik der Ladungsträger und stellen Unterschiede zwischen den Architekturen heraus. Dabei können wir ähnliche Prozesse feststellen welche aber langsamer in den planar Zellen ablaufen.
Aus diesem Vergleich können wir schließen, dass die schwächere Ausprägung von langsamen Prozessen in mesoporösen Zellen ein Grund für deren geringere J-V Hysterese ist.

Abstract

Perovskite solar cells are a novel class of solar cells that have shown a rapid progress during their development. In the course of this development, the effect of J-V hysteresis was found which is not present in other solar cell types. There is scientific consensus, that points out migration of mobile ions in the perovskite absorber as a reason for this J-V hysteresis. This ion migration is linked to response on the time scale of milliseconds.

The method of kelvin probe force microscopy (KPFM) has been shown to be able to measure charge carrier movements, both locally and temporarily. In the first part of this thesis we will estimate the temporal resolution of our KPFM setup and point out which time scales are within the range of our resolution.

To be able to measure KPFM on solar cell samples, nanometre flat cross sections of the cell are necessary. In the second part of this thesis we will develop and characterise a novel milling method, based on a method by Weber et al. [1]. This method utilises a Hitachi IM4000 milling device. We show that we can prepare large cross section areas with this method within hours.

In the third part of this thesis, we will comparatively test this Hitachi method on a mesoporous and a planar perovskite solar cell architecture. These two cell types show different degrees of J-V hysteresis. Within our comparison we investigate charge carrier dynamics and highlight differences between the cell architectures. At the end of this comparison we find that similar processes happen in both cells, however slower in the planar cells.
From this comparison we can argue that the slow processes linked to hysteresis are less pronounced in mesoporous cells. We conclude that this is one source for the lack of hysteresis in mesoporous cells.

1. Introduction

On earth, the most abundant and only infinite[1] energy source is radiation from the sun. All other sources, mainly fossil and nuclear, are finite and with today's technology could be depleted within 500 years[2]. At the same time the worlds energy consumption is ever increasing. This in itself is reason enough to push research to develop more efficient solar cells to harness the sun's energy.
The first modern solar cell was developed by Russel S. Ohl in 1941 at the Bell Laboratories[3], the same laboratories that developed the first transistors. From his experiments on p-n junctions he found, rather by accident, that when illuminated, silicon generates a current. Still today, p-n junctions are the most common way to separate the charges generated by absorption of photons (further details in ch.2). The facile realisation of p-n junctions in silicon by doping has lead silicon solar cells to become the predominantly used technology[4]. This is not to say that research into other solar cell technologies was fruitless. The use of other elemental semiconductors like GaAs and CdTe yields efficient cells as well. These materials occur however less abundant as silicon on earth and are more expensive. Since 2000, an emergent technology have been organic solar cells made from organic compounds. They have the potential to be a low cost alternative to silicon cells, but have to deal with low stability and efficiency yet. These technologies cannot compete with the head start of silicon solar cells and their advanced manufacturing methods though.
In 2009 however, a promising contender to silicon solar cells arose, namely perovskite solar cells (**PSC**). Within a decade their conversion efficiencies went, starting from $\approx$3% in 2009, to 23.7% as of today and have surpassed the industrial standard, multicrystalline silicon cells. The main advantages of PSCs are their low cost production and the tuneability of their band gap, making them ideal candidates for tandem solar cells (further details in ch.3).
PSCs exhibit effects that have not been found in common silicon solar cell, one prominent being the hysteresis in J-V curves used for measuring the efficiency. The processes that lead to this hysteresis are not fully explained yet. An approach to elucidate the underlying processes involves looking at the microscopic properties of working solar cells. The local dynamics of charge carriers such as electronic or even ionic charges might explain what processes come together to cause hysteresis.

[1] Considering the sun might live on longer than life on earth has existed[2]
[2] `https://www.scientificamerican.com/article/how-long-will-global-uranium-deposits-last/`, last access 26.02.2019

A method that rose quickly to significance, for measuring microscopic features is the atomic force microscopy or **AFM**. AFMs work by tracking the forces (e.g. electrostatic forces) acting on a cantilever with a nanometre fine tip. Thus, it is an ideal candidate for measuring charge carrier dynamics as one can investigate surfaces with a nanometre resolution. Furthermore it is possible to measure electric properties with a variant of AFM, called KPFM. More details on these methods are explained in ch.4.
For KPFM measurements it necessary that the surface is flat. This poses a challenge since solar cells have to be broken to expose all layers and to get a look inside the cell with AFM. The surface of the broken cell however is usually rough on a micrometre scale. Weber et al. developed a method to tackle this challenge. They used a focused beam of gallium ions and polished the surface via sputtering [5]. The results are nanometre flat cross section where KPFM measurements are feasible. It is unknown though what effect this preparation method has on the solar cell. The milling with gallium ions is a rather uncharted process and there is the possibility that the resulting surface does not show all of the original properties of the cell.
We thus can identify two gaps of knowledge:

- What dynamic effects can be identified on a microscopic scale that lead to hysteresis in PSC?
- What effect has the milling preparation on the cross sections?

In this thesis we aim to investigate these two questions. For this purpose, we apply a novel milling technique working with argon ions, for the preparation of PSC cross setcions (see ch.7). This new method is supposed to be less damaging due to the usage of less reactive argon ions. We will compare both milling techniques to find out what effect they have on PSC cross sections (see sec.8.2). At the end of this comparison we will evaluate which method is more suitable.
The method we use to analyse these cell cross sections is AFM, respectively KPFM. We will use a time-resolved version introduced by Weber et al. [1]. For this we will first determine the temporal resolution of our KPFM setup (see ch.6). Within the temporal resolution of this method we will analyse the charge carrier dynamics in PSC and give possible reason for the sources of hysteresis (see sec.8.1).

Part I.

Theory

2. Concepts in Solid State Physics

The field of solid state physics is a vast field that has propelled a lot of today's technologies. This chapter serves the purpose to shed light on some of the concepts used in this work. Especially those necessary to understand the working principles of a solar cell, the contact potential present in KPFM and the mechanisms underlying sputtering will be explained.

2.1. Electronic Band Structures

The description of electron energy levels for solids is different from that for single atoms due to the crystal periodicity and large numbers of atoms involved. This leads to a **band structure** of energy states instead of discrete levels. The most prominent of these bands are the valence and conduction band which together are responsible for the majority of electronic and optical properties of a material. The following description applies to crystalline solids, but its qualitative results hold also for other solids.
We start the description with the single electron approximation, meaning we will look at a single independent electron that feels the potential $V(r)$ which is generated by all atoms of the solid. This potential thus has the periodicity of the lattice:

$$V(r) = V(r + R) \tag{2.1}$$

with a lattice vector R. To get the energy states of this system we have to solve the Schrödinger equation:

$$E\Psi(r) = H\Psi(r) = \Big[-\frac{\hbar^2}{2m}\nabla^2 + V(r) \Big] \Psi(r) \tag{2.2}$$

where $\Psi(r)$ is the wave function of the electron which is spread over the whole lattice. Felix Bloch was the first (1928) to propose a solution where a plane wave is superposed with a modulation that has the periodicity of the crystal lattice:

$$\Psi_k(r) = \sum_G C_{k-G} e^{i(k-G)\cdot r} = \frac{1}{\sqrt{N}} \sum_R e^{ik\cdot R} w(r - R) \tag{2.3}$$

where G are reciprocal lattice vectors, k the momentum vector, C_i Fourier coefficients, N the number of unit cells and w so called Wannier functions. Both terms describe the same wave, so called bloch waves, the first in reciprocal and the latter in real space.

Inserting Ψ_k into the Schrödinger equation we can see that the energy dispersion relation $E(k)$ has the same periodicity as the lattice

$$E(k) = E(k + G) \tag{2.4}$$

For the specific derivation of the full dispersion relation $E(k)$ many model approaches exist that try to approximate the components C_i and $w(r - R)$ to get the solution Ψ_k. We will qualitatively describe one of them, the tight binding model. In this approach we go from isolated atoms together with their electrons and slowly bring them closer until they take their lattice positions. We then can approximate Ψ_k as a linear combination of the original atomic orbitals and substitute $w(r - R)$ for an orbital $\phi_n(r - R)$ where n stands for the n-th energy level. When the atoms get closer the initial discrete energy levels will split up into N close energy levels (N being the number of unit cells). For an infinite crystall ($N \to \infty$) we get a continuous band of energies, which is a good approximation for real macroscopic crystals. We thus get a dispersion relation $E_n(k)$ where n is a band index and k a momentum vector that can be limited to the first Brillouin zone due to the periodicity of the lattice. In this model the actual position and width of the energy bands depends on the orbitals that constitute them and if the bands are not wide enough (as is the case for less overlapping orbitals) they are separated by a gap of prohibited energy states. We now see the origin of the term band structure, referring to bands of allowed and prohibited energy states. An example is shown in fig. 2.1 for pure silicon.

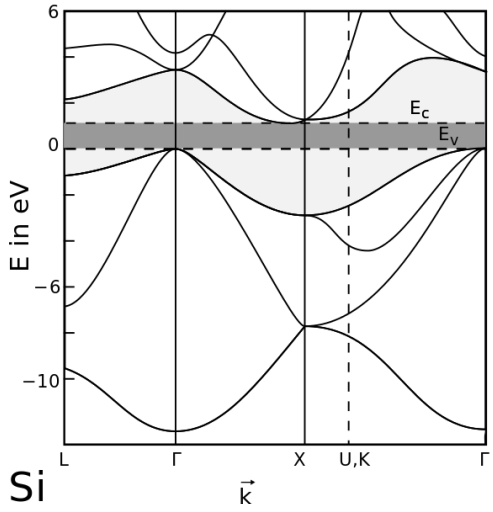

Figure 2.1: Schematic of the band structure of Silicon. On the y-axis the zero energy point was taken to be the upper edge of the valence band. The x-axis shows momentum space with reciprocal lattice points. Grey highlighted is the band gap.
Source:[6], revised by [7]

To understand what makes a solid an insulator, semiconductor or conductor we have to look at the **Fermi energy** and how the energy bands are filled up. If we set the lowest possible energy level to zero and from there, fill up the energy levels with all available crystal electrons, the highest energy we get (at abolute zero, T=0K) is defined as the Fermi energy E_f . This means if the system is in its ground state, the Fermi energy will divide occupied and unoccupied states. The electronic properties of a material are dominated by those energy bands close to E_f. We distinguish between energy bands

with energies below E_f which are called **valence bands** (although commonly the band directly below E_f is referred to as "the" valence band) and energy bands which include energies $E_n(k) \geq E_f$ that are called **conduction bands**. This distinction comes from the fact that electrons in valence bands cannot transport charges through the crystal. Reason for that is for a current to flow we need to give the electrons additional momentum δk. Since the valence bands are however completely filled there are no energy states $E_v(k)$ (v being an index of a valence band) the electrons could move to without violating the Pauli principle. Materials where E_f lies in between a conduction and valence band are thus typically isolators/semiconductors (see fig.2.2). For an isolator/semiconductor to be conductive we would have to provide energy for an electron to jump from the valence band to the conduction band, where plenty of free energy states exist. The energy difference between valence and conduction band is referred to as the **band gap (energy)** and electrons can be exited to the conduction band by photons that have at least the energy of the band gap. When this happens, the electron leaves behind a positively charged vacancy which is called a **hole**. Both, electrons and holes contribute to the conductivity of semiconductors. The difference between isolators and semiconductors is a gradual one depending on the size of the band gap. Typically, the line is drawn at energies of short wave ultraviolet photons (≈5eV). Semiconductors have lower band gaps where electrons can even be excited thermally to the conduction band.
The other class of materials are semi-/metals. Here E_f lies inside an energy band. Since this band is not fully filled electrons can easily gain momentum and change to a higher energy state close-by via electric fields. Thus theses materials are conductors.

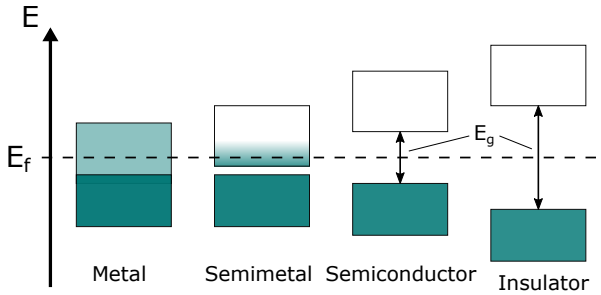

Figure 2.2: Energy diagram schemes for different types of materials. The lower darker bands indicate fully filled valence bands. Paler shades indicate partial filling in conduction bands. For semiconductors/insulators the band gap is indicated

For a more rigorous description the reader is referred to the plethora of solid state physics introduction books, of which especially [8] made the basis for this chapter.

2.2. P-N junctions in Solar Cells

In the previous section we learned that in semiconductors, where the band gap small is, electrons can be excited to the conduction band through the absorption of photons with $E \geq E_g$. The energy the electrons receive can be harvested if they are given a direction to travel to, thus yielding a current. This is the working principle of a solar cell.
Practically this can be achieved by **doping** semiconductors to get a **p-i-n junction**.

Doping is the controlled process of incorporating impurities (dopants) into a semiconductor. The dopants locally modify the band structure of the semiconductor by introducing additional energy states and two types can be differentiated: The first is n-type doping, where the states appear near the conduction band. This leads to an increased number of free electrons, as they can be more easily excited thermally. The additional states go hand in hand with shifts in the respective Fermi energies as depicted in fig.2.3. The second type is p-type doping where additional states appear near the valence band and the Fermi energy is shifted to the valence band. Analogue, there is an increased number of free holes.

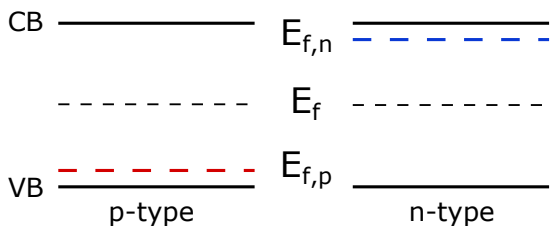

Figure 2.3: Fermi energies in doped semiconductors. For n-type doping the modified Fermi energy is near the conduction band edge (blue). Electrons can be excited here with minimal energies. For p-type doping we have the opposite case of a Fermi energy near the valence band edge (red).

A **p-n junction** is a transition from a p-type to a n-type doped region. At the interface where the different regions meet is a concentration gradient of free charge carriers. This gradient leads to a diffusion of electrons from the n-type to the p-type region. The resulting charging of the regions near the interface leads to an electric field opposed to the drift direction. This field is called the **built-in field** of the p-n junction.

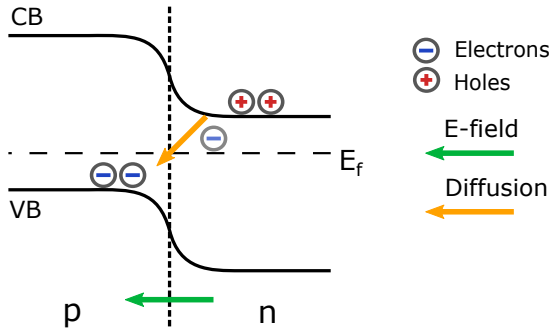

Figure 2.4: Scheme of a p-n junction in equilibrium. Fermi energies align at the junction. Electrons diffuse from the n-type region to the p-type region and leave behind holes. The resulting built-in field generates a drift that is in equilibrium with the charge diffusion.

In solar cells this built in field is what drives excited electrons in one direction, from p- to n-type region. At the same time, the n-type region acts as a membrane that is mostly permeable for electrons. Analogue this applies to holes in the p-type region. For the detailed working principles of solar cells and p-n junctions the reader is referred to [8, 9].

2.3. Contact Potential Difference

Another effect that can be explained with the concept of Fermi energies is the contact potential difference (**CPD**). It is the potential difference that arises when two conductive materials are brought into electrical contact. If the materials have different Fermi energies, electrons will move from the material with the higher Fermi energy to the one with the lower, and while doing so will leave surface charges of opposite signs on the respective materials. This happens until the resulting potential between the two materials is equal to the difference in their work functions

$$e\phi = W_1 - W_2 \tag{2.5}$$

The **work function** W is the energy it takes to remove an electron from a solid into the vacuum nearby according to

$$W = E_{vac} - E_f \tag{2.6}$$

and hence depends on the materials Fermi energy.

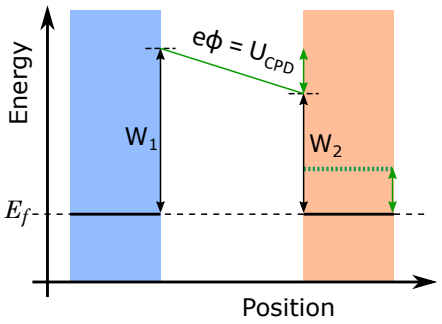

Figure 2.5: Energy levels for separated materials in vacuum and for materials in contact. Green dotted is the Fermi energy of material two when separated. The green arrow indicates the shift of the vacuum energy for material W_2

The CPD can change when the materials are disturbed out of equilibrium. This happens for example when a semiconductor is illuminated with photons with energy higher than the band gap. The photons excite electrons into higher bands, disturbing the equilibrium state. This leads to the mentioned change in CPD and the difference between dark and illuminated CPD is defined as the **photovoltage**.

2.4. Sputtering

Sputtering is the process of erosion of a target material through bombardment of high energy ions. It has found usage in the field of surface physics for the manipulation/preparation of nanometre fine surfaces. To visualise the process one can take the analogy of a game of pool: a high energy ion impinges on the atoms at the material surface, similar to the starting shot of the white ball. Through elastic scattering the target atoms get in motion and the majority of the ion's momentum is transferred into the bulk solid. Statistically some atoms especially near the surface will recoil out of the bulk (if their energy is higher than the binding energy) leading to a depletion.

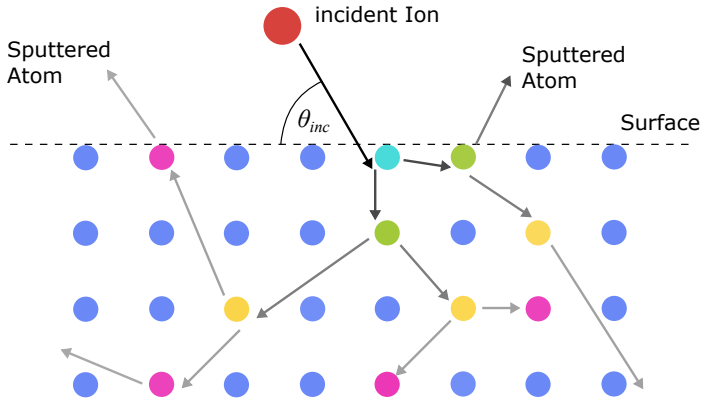

Figure 2.6.: Schematic of Sputtering. The incident ion(red) carries momentum that is transferred into the bulk(blue). Colours indicate primary(cyan), secondary(green), tertiary(yellow), quarternary(purple) scattered atoms. Arrows indicate transfer of momentum, paler shades meaning less momentum

The latter recoiled atoms are also referred to as being **sputtered**.
The theoretical base was largely laid by Sigmund [10, 11]. In it one central term is the **sputtering yield** Y, which is the rate of sputtered atoms per incoming ion. It is thus a measure for the erosion efficiency. The sputtering yield depends on several factors, mainly the ion acceleration energy E_{acc}, the material of ions and target atoms (described here with a parameter $C_{ion-atom}$), as well as the incident angle of the ions to the surface θ_{inc} [12]:

$$Y = Y(E_{acc}, C_{ion-atom}, \theta_{inc})$$

To knock an atom out of a solid one has to bring up at least the binding energy. Sputter yields however stay low even for energies orders of magnitude higher than the binding energy [13]. This shows that most of the ion energy does not go into sputtering but into heating of the material and generation of defects in the solid. To reduce the impact of sputtering on samples one therefore has to either reduce the flux of energy by decreasing the incident ion beam current or increase the sputtering yield. The first leaves the sample time to cool down. The second way can be done by choosing an incident angle θ_{inc} that gives maximal sputter yield. For shallow angles the ions transfer less energy as they rather ricochet off the surface, thus leading to few sputtering events and a low sputtering yield. The other extreme of perpendicular incidence leads to maximum energy transfer. Here however the transferred momentum is opposite to the direction atoms need to go to be sputtered, thus reducing the sputtering yield. Wei et al. showed that angles around 70° lead to maximum sputtering yield.

2.5. Lock-In Amplifier

Lock-In amplifier (short **LIA**) are a type of narrow bandpass filters, that can filter out noise from periodic signals. The working principle is that the noise loaded signal

of interest is mixed with an ac reference signal and filtered through a low pass filter. The effect is that the LIA calculates the cross-correlation of input and reference which is maximal when input and reference frequency are equal. For the ideal case of a sinusoidal input and reference we can calculate the output as:

$$U_{out}(t) = \frac{1}{T}\int_{t-T}^{t} \sin(\omega\tau + \Delta\varphi)U_{in}(\tau)\, d\tau \tag{2.7}$$

So called single-phase LIA only retrieve the signal amplitude with this method. More advanced dual-phase LIA are also able to calculate the phase of the signal with respect to the reference. They do this by copying the signal path for a reference signal that is phase offset by 90° (see fig.2.7). Through trigonometry the phase can be calculated as $\phi = \arctan(\frac{U_{out,90°}}{U_{out,0°}})$.

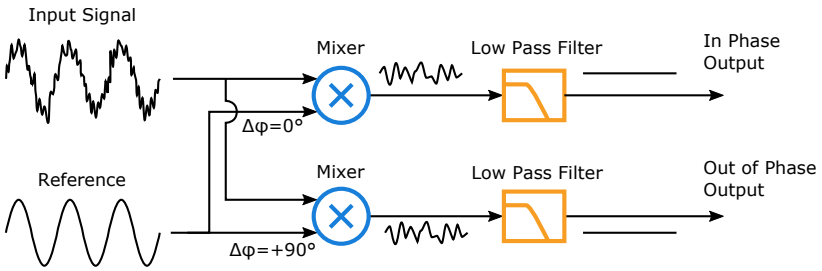

Figure 2.7.: Schematic of a dual-phase LIA. After the mixer the signal has components $\omega_{in} - \omega_{ref}$, $\omega_{in} + \omega_{ref}$ as well as noise. The latter two are filtered out by the low pass filter.

The temporal resolution of a LIA, i.e. how fast it reacts to amplitude changes of the input oscillation, depends on its **bandwidth** which is the inverse of the integration time $BW = \frac{1}{T}$. Thus to measure dynamic changes in the signal amplitude that happen on a timescale T_{sig} the bandwidth has to be chosen $BW \geq \frac{1}{T_{sig}}$. Higher bandwidths however go along with increased noise levels that limit the discrimination between signal and noise. In a similar context the bandwidth is central to signal processing theory. Here it describes the window of frequencies around a carrier that can be analysed.
For further details on implementations and the noise characteristics of LIA see [14].

2.6. PID Feedback Control

Systems where a control variable $c(t)$ regulates a process variable $p(t)$ can be controlled with a feedback loop. Feedback compare the instantaneous variable $p(t)$ with a desired value (or **setpoint**) $s(t)$, yielding an error variable $e(t)$ that indicates how far off $p(t)$ is. The error is then used to calculate a new $c(t)$ so that the system yields the desired output $p(t) = s(t)$.
One class of feedbacks are PID feedbacks. Here $c(t)$ is calculated as the sum of three

control terms which are proportional to : $e(t)$ itself, to the **i**ntegral of $e(t)$ and to the time **d**erivative of $e(t)$ according to:

$$c(t) = K_P\, e(t) + K_I \int_0^t e(\tau)d\tau + K_D \frac{de(t)}{dt} \tag{2.8}$$

Hence the name PID feedback. The weights K, commonly called **gains**, have to be adjusted to the system response.

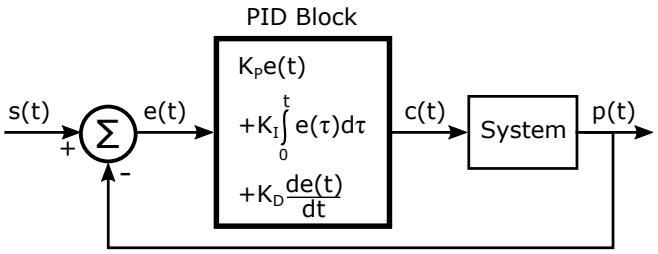

Figure 2.8: Schematic of a PID feedback

For low gains (small K) the feedback response $c(t)$ is small even if the error signal is large which makes the feedback slow in following changes. The opposite happens for high gains: the feedback reacts violently to even small changes and overshoots the desired value. If gains are set to high, PID feedbacks even become unstable and start to oscillate. A scheme is shown in fig.(A.2). Ideally the gains are set so that they result in little overshoot until the systems reaches the set point. The overshoot is accepted in return for a quick response to changes.

3. Perovskite Solar Cells

Perovskite solar cells (**PSC**) are a group of photovoltaic devices (**PV**) that have a hybrid inorganic-organic absorber in common which crystallise in the perovskite crystal structure. Perovskites as PV absorbers entered the scientific stage in 2009 [15] when the perovskite material was first used in dye sensitized solar cells (DSSC). Interest soared when they were used in solid state solar cells and efficiencies instantly rose from 3% to ≈10% and above [16, 17]. Here the typical cell architecture consist of the perovskite absorber sandwiched between two charge selective contacts which are surrounded by conducting electrodes (fig.3.1). The charge selective contacts together with the absorber act as a p-i-n junction and are needed to enforce a direction for currents to flow in the working cell (compare fig.A.3).

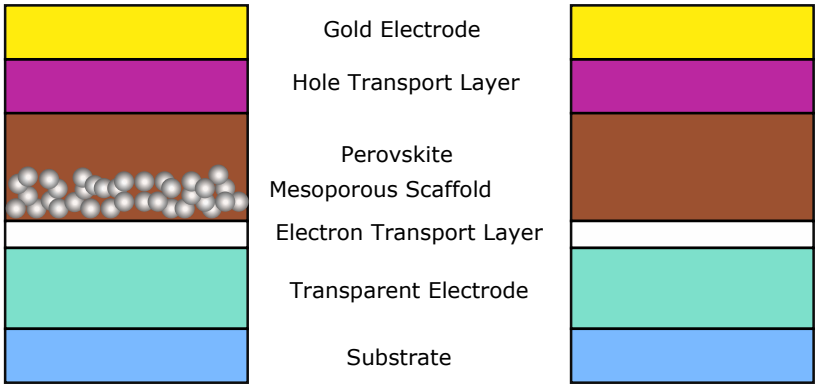

Figure 3.1.: Two PSC architectures. Left a mesoporous device where the perovskite penetrates an additional TiO_2 scaffold, right a planar device

As of today, record efficiencies of 23.7% have been reached and PSCs have long surpassed multicrystalline silicon solar cells concerning efficiency cells[1]. These top tier efficiencies are a result of the ideal properties of hybrid inorganic-organic perovskites for the use as solar cell absorbers. Amongst these are long diffusion lengths combined with high absorption of light over a large spectrum, making them ideal candidates for the use in thin film devices[18, 19]. In addition, they show highly tunable band gaps [20]. This has two benefits: First, the band gap can be shifted to give an ideal band gap according to the Shockley-Queisser limit [21]. Second, they can be easily incorporated in tandem solar cells structures. Furthermore, the perovskite absorber shows a high tolerance to crystal defects[22, 23]. Usually crystal defects lead to current losses

[1] `https://www.nrel.gov/pv/assets/pdfs/best-reserch-cell-efficiencies.pdf` , last access 26.02.2019

due to non-radiative recombination processes. For further details on the absorber see sec.3.1.
If these points are not incentive enough to manufacture PSCs, then it is the fact that they can easily be processed from solutions under low temperatures [24], resulting in low cost manufacturing. However the technology of PSCs is still in its infancy and poor stability in the presence of humidity, oxygen and UV radiation [25, 26] has yet to be overcome for PSCs to be competitive [27]. Furthermore the use of toxic lead poses a problem for commercialisation under current RoHS rules. Lead has to be either substituted or diluted by the use of another metal like tin [28, 29] so that PSCs do not pose an environmental risk.
The recent focus of research is thus in overcoming these instabilities as well as understanding effects previously not seen in other PV devices. These include slow transient responses times[30], high ionic conductivity of the absorber [31] and hysteresis in current-voltage curves (**J-V curves**) [32].

3.1. Hybrid Inorganic-Organic Perovskites

In general perovskites are crystals consisting of the chemical formula ABX_3 where A and B are cations that compensate the charge of anions X. The crystal structure is that depicted in fig.3.2 where the larger cation A is centred in a cuboid of corner sharing octahedra of ions BX. In the PV community the term perovskite has become synonym

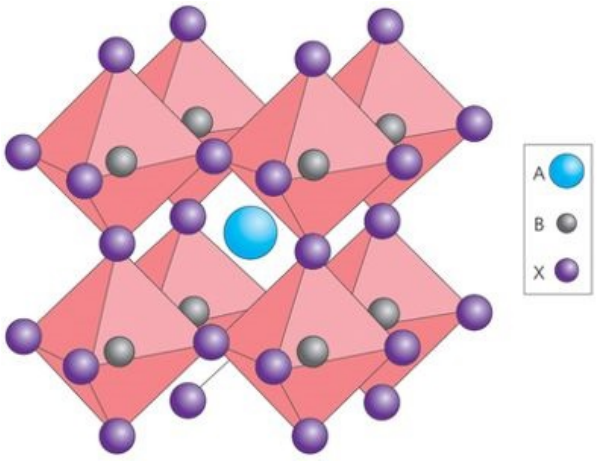

Figure 3.2: Crystal structure of perovskites, taken from [33]. Shown is a cubic phase.

with mixed metal organic halide perovskites (which will further only be referred to as perovskites). The archetype and most studied of these perovskite is methylammonium lead iodide ($CH_3NH_3PbI_3$, short **MAPbI**). Here lead and iodide take the role of the lattice ions B and X, respectively, while methylammonium ($CH_3NH_3^+$, short **MA**) takes the role of the central cation A. As mentioned before, the band gap of perovskites can be tuned. This tuning is done for example by exchanging iodine for other halides like chlorine or bromine [34, 35]. Examples for the cation A are cesium or formamidinium ($HC(NH_2)_2^+$, short **FA**) [36, 37, 35]. The most efficient PSC today

consist of a mixture of the above mentioned cations and halides [35, 38].
A peculiar property of perovskites is their ionic conductivity. Each constituent A,B,X was found to be mobile through migration of crystal defects, with activation energies below 1eV [31, 39, 22, 23]. The dominant migrating species is the halide whose mobility is increased by the formation of halide vacancies [31, 39]. In the presence of voltages across the material, as is the case in working PV devices, the migrating ions can travel along the electric field and accumulate at the electrodes. For instance in PSCs it was found that halide ions move to one electrode, leaving behind positively charged vacancies at the other electrode (or more specifically forming space seperated Frenkel defects) [40, 1]. The accumulation of these ionic charges has been proposed as the cause of hysteresis in PSCs. The hysteresis in J-V curves will be further explained in the next chapter as it will be one focus of this thesis.

3.2. Hysteresis in Perovskite Solar Cells

To estimate the efficiency of solar cells one performs J-V curves, that is sweeping through a range of voltages while recording the current output from the cell. Under illumination one can read the power the cell can produce by multiplying the current density with the voltage times the area that outputs this current. The efficiency of the cell can then be calculated by dividing the maximum obtained power P_{max} by the irradiance power P_{irr}:

$$\eta = \frac{P_{max}}{P_{irr}} = \frac{U_{max} \cdot J_{max}}{P_{irr}} \cdot A_{irr} \tag{3.1}$$

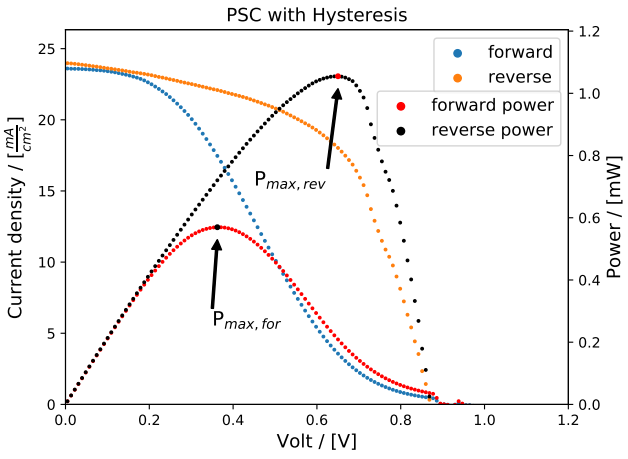

Figure 3.3: J-V curve showing hysteresis in a planar gold/spiro/triple-cation-perovskite/SnO_2/FTO PSC device. Additionally the power is plotted together with the maximum power points

Hysteresis in PV devices means the divergence between a J-V curve swept from low voltages to high (**forward curve**) and one swept from high voltages to low (**reverse curve**). For PSCs this hysteresis is not only dependent on the specific device structure but also on the cell's condition(-ing) right before recording the J-V curve [32, 41]. The

main implication of hysteresis is that it complicates finding the real efficiency of PSCs: cells might not be as efficient under real working conditions as lab measurements might suggest. Hence, one early focus of research was identifying and preventing hysteresis. A multitude of sources have been proposed for hysteresis, for instance trapping of electronic charges at the interfaces[42, 43, 44]. There is a consensus though, that ion migration is the main reason[40]. Models that explain hysteresis based on ion migration have in common that the separation of negative ions and their positive vacancies due to bias voltages leads to an additional electric field [45, 46]. This field when opposed to the internal field can hinder extraction of electrons and holes, thus impairing cell operation (see fig.3.4). Contrary, when the field is in line with the internal field, charge extraction is alleviated.

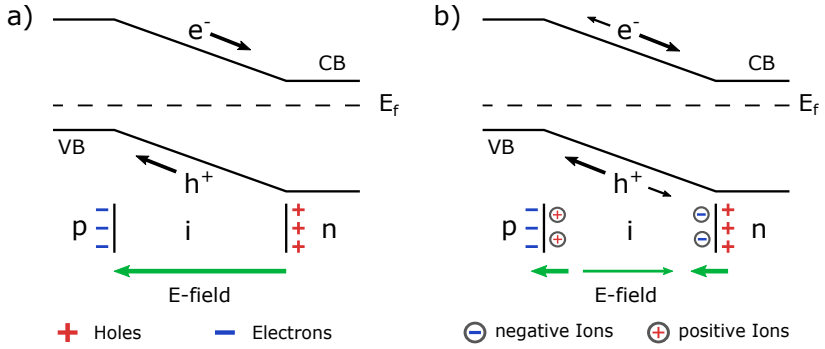

Figure 3.4.: a) Band structure across a p-i-n junction. Localised electronic charges generate a built-in electric field. b) Mobile ionic charges move along thee built-in field and partially shield it. Shown is a symmetric case with no interactions at the interfaces.

This process is often depicted as being symmetric, that means moving anions leave behind equally large positively charged vacancies and the resulting ionic field is point symmetric around the perovskite absorber centre [45, 46, 40]. However, this assumption is not consistent with the fact that changing one of the charge selective contacts can reduce or even erase hysteresis. For example it has been shown that mesoporous devices exhibit less hysteresis than planar devices, given the HTL is the same [47]. Planar devices can also be fabricated with minimal hysteresis if the metal oxide ETL is replaced with a fullerene based one [48, 49]. The assumption here is that in the hysteresis free cases ion migration is either hindered or reduced. This implies that the interfaces to the perovskite need to play a role in hysteresis that exceeds simple bulk ion migration [1]. It is thus necessary to locally understand the interplay of ions with the perovskite interfaces on scales of nanometre.
One promising candidate for locally investigating charging behaviours is AFM or rather its surface potential measuring version KPFM, which will be introduced in the following.

4. AFM

The Atomic Force Microscope (**AFM**) is arguably the most notorious of the scanning probe methods. Developed in 1986 by Binnig et al. [50] it has become one of the standard methods in surface sciences and helped push the limits of research in this field. Its strengths are the resolution of various surface properties, for example topography, hardness and potential with micrometre down to atomic resolution (under UHV [51]).

4.1. Basic Principles

As the name hints, an AFM measures forces and can do so with a resolution down to attonewtons [50]. The base for all AFMs is a cantilever with an (ideally) atomically sharp tip at its end. This cantilever can be in its simplest form described as a Hooke's spring with a corresponding spring constant

$$-k = \frac{F}{\Delta x} \tag{4.1}$$

By measuring the deflection Δx one can calculate the force F acting on the cantilever. The first AFM setup by Binnig et al. consisted of a scanning tunneling microscope (STM) which tracked the cantilever deflection by measuring the tunnel current between the STM tip and the cantilever backside.

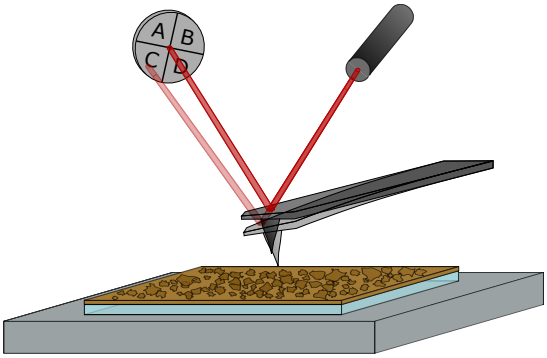

Figure 4.1: Typical AFM setup. The cantilever with its tip scans over the sample. Deflection of the cantilever results in a changed beam path (depicted transparently) from the laser to the photodiode

Nowadays a combination of a laser LED and a four quadrant photodiode is used to measure the deflection. The laser is directed at the backside of the cantilever and the reflection then captured by the photodiode (see fig.4.1). This setup is calibrated so that the reflex hits the middle of the photodiode, yielding ideally the same voltage output U from all four quadrants. Through interaction with the sample surface the cantilever will bend (depending on the forces acting, see further sec.4.2), causing the

reflection to shift along the four quadrant photodiode. This shift leads to a voltage drop in those quadrants which are less illuminated and vice versa a rise in voltage for those that are illuminated more. These changes thus lead to a voltage difference ΔU (for simplicity we take the 1-D case). To connect the voltage ΔU to a real deflection of the cantilever one has to make a calibration to get the so called inverse optical lever sensitivity (Invols). The Invols (dimension $[\frac{m}{V}]$) translates the measured voltages into a real deflection according to

$$\Delta x = Invols \cdot \Delta U$$

This parameter can be calculated from the thermal motion of the cantilever at its resonance frequency [52, 53]. Finally the deflection gives us with eq.(4.1) the force acting on the cantilever.
To get an image of a surface property, like the topography, one scans in a pixel grid over the surface while keeping a quantity, for example the force, constant. This is achieved with the help of a feedback loop, which drives piezo actuators to change the tip-sample distance until a predetermined force acts on the tip. The control output of the feedback at each pixel point corresponds to the height at these pixels, resulting in a rasterised image of the region of interest.
This working mode is also called contact mode as the tip stays in constant contact with the surface while scanning. More sophisticated modes will be discussed in sec.4.3.

4.2. Forces in AFM

The net force acting on the tip is a superposition of several forces, each with their own distance dependence [54, 55, 56]. To perform AFM and analyse the data it is thus important to know the contribution of each force constituent depending on the distance between surface and tip. Here we focus on forces primarily acting in an AFM setup in air where at least one of the participants, tip or sample, is conductive. We can distinguish the acting forces between the range where they are the dominant force.

4.2.1. Short Range - Pauli Repulsion

For distances below 1nm tip and sample get so close that the electron wave functions of the closest atoms overlap. This can lead to attractive forces when the overlap is energetically favourable similar to chemical bonds. However, increasing the overlap beyond such a point leads to a repulsive force due to the Pauli repulsion principle. The electrons as fermions cannot take on the same state and thus resist further approach through a repulsive force.

4.2.2. Medium Range - Van-der-Waals Forces

Van-der-Waals forces are the forces that atoms and molecules exert onto each other due to the presence of electric dipoles [57, 58]. They are most significant for distances $\mathcal{O}(1 - 10nm)$ and can be subdivided into three categories:

- Keesome interactions: These describes forces that molecules with permanent dipoles (for example water) exert onto each other.
- Debye interactions: A molecule with a permanent dipole induces a dipole in an otherwise neutral atom/molecule leading to an attractive force.
- London (dispersion) interactions: Fluctuations of the electron cloud around neutral atoms/molecules lead to temporary dipoles which then interact with each other.

Van-der-Waals forces are mostly attractive due to the alignment of the dipoles. For larger distances, the time it takes for a photon to travel from dipole to dipole and mediate the interaction grows larger than the time the temporary induced dipoles exit. This effect, also called retardation effect, adds to the decay of Van-der-Waals forces for distances beyond $\mathcal{O}(1-10nm)$[54].

4.2.3. Long Range - Electrostatic Forces

Electrostatic forces become significant when there is a potential U between tip and sample. This is the case when an insulating sample is electrostatically charged. For conductive materials the above described contact potential difference, which can take on values in the volt range, becomes important. We can quantify electrostatic forces by considering the tip-sample system to be a capacitor with distance dependent capacitance. For a capacitor we get the stored electric energy and the resulting electric force as:

$$E_{el} = \frac{1}{2}C(z)U_{tot}^2 \qquad \left|\frac{d}{dz}\right. \tag{4.2}$$

$$F_{el} = \frac{1}{2}\frac{\partial C(z)}{\partial z}U_{tot}^2 \tag{4.3}$$

Unlike the previous mentioned forces, electrostatic forces can be exerted by the full cantilever not only the tip apex atoms, a consequence of the long range of the forces. Electrostatic forces are important as they are the basis for measuring electrical properties with an AFM with the help of advanced working modes described in the next chapters (sec.4.3.2).

4.3. Working Modes

The abilities of the AFM quickly progressed after its development. Not only was the resolution enhanced with refined topographical imaging methods, but new imaging techniques allowed the measurement of additional observables (e.g. magnetic, electric, ferroic properties to mention a few). This is a result of the fact that every interaction that mediates a force can be measured with an AFM. From these techniques, the ones used in this work are further explained.

4.3.1. Dynamic Modes

Although force reconstruction is straightforward in contact mode, it had a few drawbacks like fast degradation of the tip while measuring. Most of the advanced AFM techniques work in dynamic modes. Here the motion of the cantilever is modulated, usually with a sinusoidal at the cantilever resonance, meaning we have several parameters (amplitude,frequency,phase) we can infer tip sample interactions from.
Since the cantilever resembles a springs, it can also be excited to oscillate. Mathematically this can be described by a driven harmonic oscillator:

$$\frac{k}{\omega_0^2}\ddot{z} = -kz - \frac{m\omega_0}{Q}\dot{z} + F_{ts}(z) + F_{ext}(t) \tag{4.4}$$

with Q being the quality factor of a damped oscillation, m the spring mass, ω_0 the cantilever resonance frequency, F_{ts} the tip-sample forces and F_{ext} the external driving force. For an oscillator, information about interactions is saved in parameters like amplitude, frequency and phase of the oscillation. The dynamic modes aim to demodulate the interactions by looking at one of these parameters and are commonly labeled by the parameter in focus plus 'modulation' [59, 60, 61]. In amplitude modulation (**AM**) a feedback drives the tip-sample distance to keep the oscillation amplitude to a set point. In frequency modulation (**FM**) the same applies for a feedback that keeps the resonance frequency constant. The theoretical background for both methods has been summarised by García, Pérez and Giessibl [62, 63], so only key results will be mentioned.
Far from the surface the can be described as a damped harmonic oscillator and tip-sample forces can be put to zero $F_{ts} = 0$. If we consider a sinusoidal excitation $F_{ext}(t) = F_0\cos(\omega t + \phi)$ the solution of eq. (4.4) can be calculated as a superposition of an exponentially decaying and a steady solution. After a settling time the steady solution will dominate with the driving frequency ω dependent amplitude

$$A_{free}(\omega) = \frac{F_0/m}{\sqrt{(\omega_0^2 - \omega^2)^2 + (\frac{\omega\omega_0}{Q})^2}} \tag{4.5}$$

and the cantilever will oscillate with a phase offset ϕ with respect to the driving force according to:

$$\tan(\phi) = \frac{\omega\omega_0/Q}{\omega_0^2 - \omega^2} \tag{4.6}$$

A high signal-to-noise ratio is thus achieved by maximising the amplitude by setting the drive frequency equal to the cantilever resonance $\omega = \omega_0$. When we now include tip-sample forces we can write the total acting force and the resulting effective spring constant as:

$$F = F_0 + \left(\frac{dF_{ts}}{dz}\right)_{z_0}(z - z_0) \qquad \left|\frac{d}{dz}\right. \tag{4.7}$$

$$k_{eff} = \left(k - \frac{dF_{ts}}{dz}\right)_{z_0} \tag{4.8}$$

With the effective spring constant we obtain a new effective resonance frequency in the presence of tip-sample forces:

$$\omega_{eff} = \sqrt{\left(k - \frac{dF_{ts}}{dz}\right)/m} \tag{4.9}$$

Tip-sample forces thus induce a resonance frequency shift that is dependent on their gradient. The changed effective resonance also leads to a new resonance curve when we substitute ω_0 for ω_{eff} in eqs. (4.5) and (4.6) (see fig.4.2)

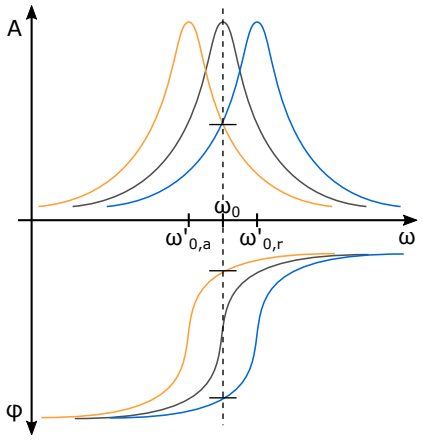

Figure 4.2: Shift of the resonance and phase curves in the presence of forces F_{ts}. Orange stands for a mean attractive interaction, blue for a repulsive one. The horizontal bars indicate the shift in phase and amplitude when continuing to drive with ω_0

From this approximation we can qualitatively see that tip-sample interactions attenuate the amplitude when we continue to drive at ω_0.
AM modes control the amplitude commonly with a lock-in amplifier (see fig.4.3), a device that acts as a narrow bandpass detector. By setting its reference frequency to the drive frequency ω, changes in the oscillation amplitude can be measured with a high signal-to-noise ratio. The amplitude can then be used as the control parameter for the height feedback.
Since AM AFM is used as the only topographical method in this work the reader is referred to reviews by Giessibl and Garcia on details about FM AFM [63, 62].

4.3.2. EFM and KPFM

A particularly important role can be attributed to measuring electrostatic forces with an AFM. These can be for example a result of differences in surface potentials between tip and sample, local charge distributions or plain biases applied to the tip/sample. Hence two methods have evolved to also be able to characterise electrical properties of samples, the electrostatic force microscopy (**EFM**) and from it further developed the Kelvin probe force microscopy (**KPFM**).
Both methods have in common that they work in dynamic modes and that the tip-sample system is regarded as a capacitor. We thus can use eq.(4.3):

$$F_{el} = \frac{1}{2}\frac{\partial C}{\partial z}U_{tot}^2$$

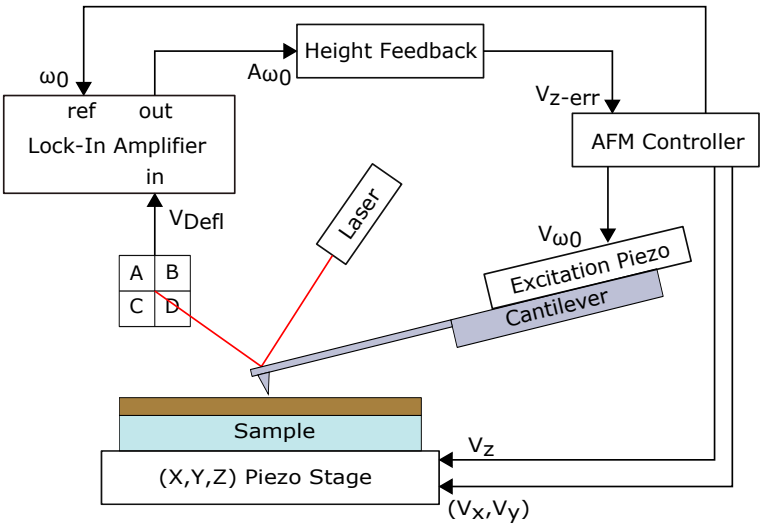

Figure 4.3.: A basic setup of amplitude modulation AFM

Here U_{tot} is the total voltage between tip and sample and is the sum of applied dc and ac biases U_{dc} and U_{ac} as well as the voltages that are pre-existent in the tip-sample system U_{sys}:

$$U_{tot} = U_{dc} - U_{sys} + U_{ac}\sin(\omega_{ac})$$

To be able to apply these biases, tip and samples have to be sufficiently conductive and in contact, or at least share a ground. For this purpose tips with conductive coatings are typically used. On the sample side this means that EFM/KPFM can only give qualitative not quantitative results for insulators.
The most significant of the system inherent voltages U_{sys} is the contact potential difference U_{CPD} described in sec 2.3. Besides the CPD, system voltages can result from unshielded charges. They can play a big role when for example mobile ionic charges are present in the sample that accumulate to generate strongly charged regions. For simplicity we now restrict the system inherent voltages to the CPD ($U_{sys} = U_{CPD}$). This is the case for uncharged samples. In ch.8 we will see samples where these unshielded charges play an important role.
Inserting U_{tot} now in the equation for the force (4.3) one yields the central equations for all EFM and KPFM methods:

$$F_{dc} = \frac{1}{2}\frac{\partial C}{\partial z}\left((U_{dc} - U_{CPD})^2 + \frac{1}{2}U_{ac}^2\right) \tag{4.10}$$

$$F_{\omega_{ac}} = \frac{\partial C}{\partial z}U_{ac}\left(U_{dc} - U_{CPD}\right)\sin(\omega_{ac}) \tag{4.11}$$

$$F_{2\omega_{ac}} = -\frac{U_{ac}}{4}\frac{\partial C}{\partial z}\cos(2\omega_{ac})^2 \tag{4.12}$$

It can be seen from eq. (4.11) that information on the CPD lies in the force term at ω_{ac} in form of the amplitude of the sinusoidal. Thus by exciting the cantilever

electrically and recording the cantilever oscillation one can measure the CPD. EFM methods focus on quantifying the amplitude of $F_{\omega_{ac}}$, whereas in KPFM one tries to minimise the amplitude of $F_{\omega_{ac}}$ by putting the dc bias $U_{dc} = U_{CPD}$.
An advantage of EFM is that no additional feedback loop is needed to compensate the CPD, like it is needed in KPFM. As a drawback, the force term at ω_{ac} will be superposed to the topography image resulting in crosstalk between the real topography and electrostatics. To circumvent this obstacle, often EFM measurements consist of two runs. In the first run the topography is imaged with the tip close to the sample. In a second run the tip is lifted slightly above the surface, where near range forces like Van-der-Waals forces can be neglected, to only map electrostatic forces. A downside is that the larger distance leads to an averaging of electrostatic forces below the tip and with it a loss in lateral resolution.
The main advantages of KPFM are the simultaneous imaging of topography and CPD and that it is more quantitative than EFM. The latter is because it obtains directly values for U_{CPD} while minimising $F_{\omega_{ac}}$. EFM is only in so far quantitative in that it gives a value for the amplitude of $F_{\omega_{ac}}$ that is proportional to $\frac{\partial C}{\partial z}$. The gradient of the capacitance on the other hand is hard to quantify as it depends on several variables like distance, materials as well as tip shape. It is known that the tip shape can change whilst measuring due to abrasion or dirt that is picked up and with that changing the tip-sample capacitance dramatically. Thus KPFM has become the predominantly used method.
The importance of KPFM for this work is that it is able to map local potential changes in a solar cell. Especially the change in the photo voltage (for term see section 2.3) is focused on, as it gives insight on charge carrier dynamics inside the PSC.

4.3.3. Amplitude vs. Frequency Modulation KPFM

Similar to the topographical dynamic modes in sec. 4.3.1 there exist several variations of KPFM each with their own dis-/advantages which in the past have been elucidated [64, 65, 66] and the variety is still an ongoing topic of research. Thus for best results it is worth evaluating the most suitable method.

AM KPFM

The above in sec. 4.3.2 described form of KPFM applies the method of amplitude modulation. According to eq. (4.11), information on the CPD is encoded in the cantilever oscillation at frequency ω_{ac}. A lock-in amplifier measures the amplitude of the oscillation at ω_{ac} and sends the output value to a feedback that aims to set the amplitude to zero. The feedback does so by applying an additional dc voltage $U_{dc} = U_{CPD}$ to the sample. Thus, the feedback output is the current CPD value which, collected over an area, gives a map of the CPD. A circuit diagram is illustrated in fig. 4.4. Here a Kelvin controller does the job of applying the ac bias as well as serving as the feedback.
By setting $\omega_{ac} = \omega_1$ to the cantilevers second eigenmode, the KPFM setup can measure

the topography simultaneously at the first eigenmode and still achieve signal-to-noise ratio enhancement by measuring at resonance.
It has been reported that AM KPFM modes can operate with lower biases U_{ac} than comparable FM modes [67, 66]. This is an advantage for materials that are sensitive to higher voltages.

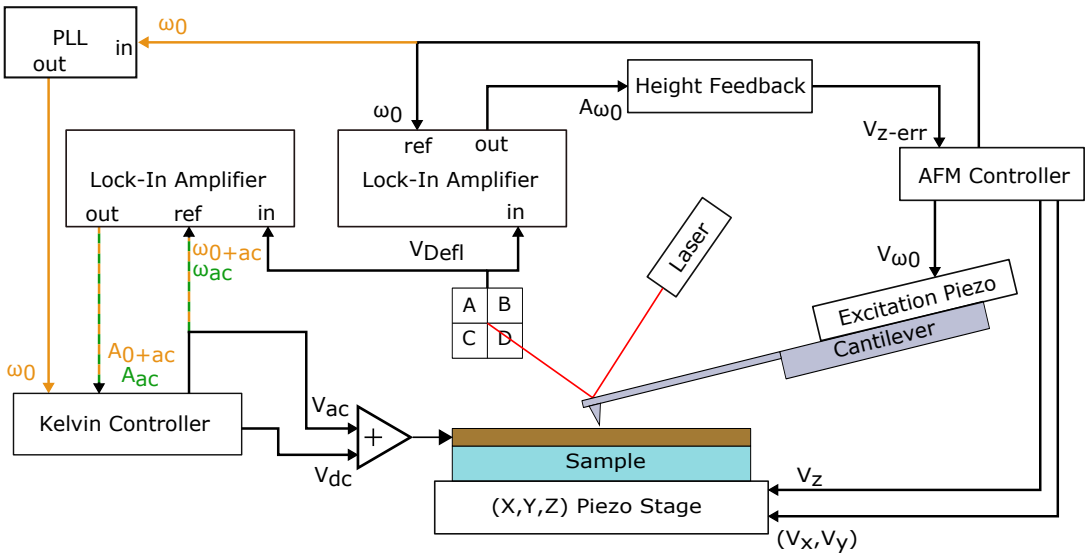

Figure 4.4.: KPFM setup. The inner green path illustrates the signal path for AM KPFM, the orange one is for FM KPFM. All other lines are shared by both methods

FM KPFM

Another way to measure the CPD with KPFM was proposed by applying the technique of frequency modulation [68]. In this model the mechanical oscillation ω_m of the cantilever is seen as the carrier signal which is then modulated by an electrical excitation of the cantilever ω_{ac}. The modulation is a consequence of the resonance frequency change of the cantilever when it is disturbed by a tip-sample interaction:

$$\tilde{\omega}_0 = \sqrt{\frac{1}{m}\left(k - \frac{\partial F_{ts}}{\partial z}\right)} \approx \omega_0\left(1 - \frac{1}{2k}\frac{\partial F_{ts}}{\partial z}\right) \tag{4.13}$$

By applying an electrical ac bias the electrical force contribution eq. (4.3) will fluctuate periodically. This gives rise to the modulated cantilever oscillation

$$z(t) = A_m \cos(\theta_i(t)) = A_m \cos\left(\omega_0 t - \frac{1}{2k}\frac{\partial F_{el}(\omega_E, t)}{\partial z} + \phi\right) \tag{4.14}$$

Where $\theta_i(t)$ is the instantaneous phase argument, ϕ a phase offset, ω_m the frequency with which the cantilever is actually driven and A_m the resulting oscillation amplitude. The oscillation $z(t)$ can then be expanded via a Fourier series where it is obvious to

see that the modulated signal will consist of the carrier frequency ω_m together with infinite pairwise sidebands $\omega_{\pm n} = \omega_m \pm n\omega_{ac}$. Practically only the first few order sidebands are considered. It can be shown [65] that the contribution of the first order

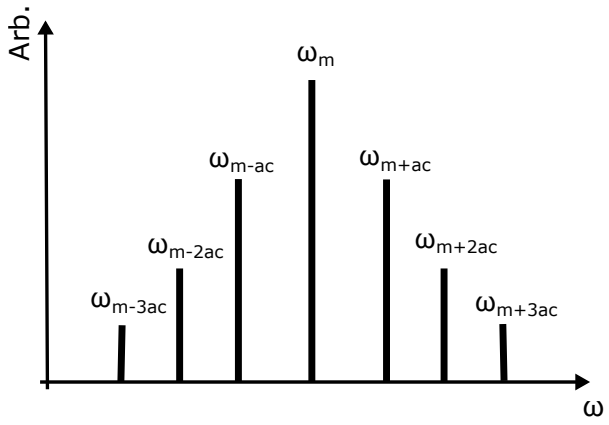

Figure 4.5: Rough scetch of the sidebands in FM KPFM. The pairwise infinite sidebands get smaller the further away from the carrier they are. Sidebands below the third order can be disregarded as they do not significantly contribute to the signal.

sideband has the form:

$$F_{\omega_m \pm \omega_{ac}} = -A_m C''(U_{dc} - U_{CPD})U_{ac} \cdot \Big[\sin\big((\omega_{ac} - \omega_m)t\big) + \sin\big((\omega_{ac} + \omega_m)t\big)\Big] \tag{4.15}$$

Similar to eq. (4.11) we can set this equation to zero by setting $U_{dc} = U_{CPD}$. In principle FM KPFM can be realised with an AM KPFM setup that tracks the frequency at one of the sidebands. A caveat however is that the sidebands also depend on the mechanical oscillation frequency ω_m, which can due to fluctuations change the position of the sidebands. To not loose sensitivity, FM setups need to rectify these fluctuations with an additional PLL that tracks the instantaneous frequency ω_m.
Besides this higher complexity, FM KPFM was shown to be the preferable mode for achieving high lateral potential resolution [64, 65]. The reason is that eq.(4.15) depends on the second derivative of the capacitance instead of the first as is the case for AM KPFM. FM KPFM is thus more sensitive for the smallest distances as can be seen when looking at the capacitance-distance proportionality of a model plate-plate capacitor:

$$C \sim \frac{1}{d} \iff \frac{\partial C}{\partial z} \sim \frac{1}{d^2} \iff \frac{\partial^2 C}{\partial z^2} \sim \frac{1}{d^3} \tag{4.16}$$

Furthermore, Garrett et al. have found a way to enhance the resolution [69] even with lower ac biases for FM KPFM. Their idea was to switch the roles of carrier and signal formally, meaning that the electrical excitation oscillation is the carrier which is modulated by the mechanical excitation. Technically one excites the cantilever electrically at $\omega_{ac} = \omega_1 - \omega_0$ and mechanically at ω_0, where ω_n is the n-order eigenmode. The result is that the sideband for FM KPFM will be at the second eigenmode ω_1 where a comparably low ac voltage is needed due to resonance enhancement. The method is called heterodyne FM KPFM. The main improvement of this technique

was however the enhanced temporal resolution for KPFM by allowing to measure with cantilevers of higher resonance frequencies [69]. This will be further elucidated in the next chapter where we highlight the factors determining the temporal resolution of AFMs.
All KPFM measurements in this thesis are performed with heterodyne FM KPFM.

4.4. Temporal Resolution with AFM/KPFM

In an AFM the signal chain from cantilever motion to a final measurement involves multiple intermediate steps of processing. In this chapter we elucidate the key steps in this process and highlight the bottlenecks where temporal resolution is lost and give an estimate for the final resolution.
In principle for an AFM, the shortest measurable time is the reaction time of an oscillator to a perturbation. For an AM setup this is determined by the speed of amplitude changes a damped oscillator can make. In FM it is on the order of an oscillation cycle to measure frequency shifts. This gives us a time constant after which an interaction can be inferred from the oscillation:

$$\text{(AM)} \quad \tau = \frac{Q}{\pi f} \qquad , \qquad \text{(FM)} \quad \tau = \frac{1}{f}$$

This shows that cantilevers with higher resonance frequencies allow for the measurement of faster processes. State of the art cantilever can have resonance frequencies in the 100kHz range with second eigenmodes in the MHz range (higher eigenmodes are in principle also measurable but yield too low SNR). The minimal temporal resolution with an AFM is thus limited to 0.1-1μs.

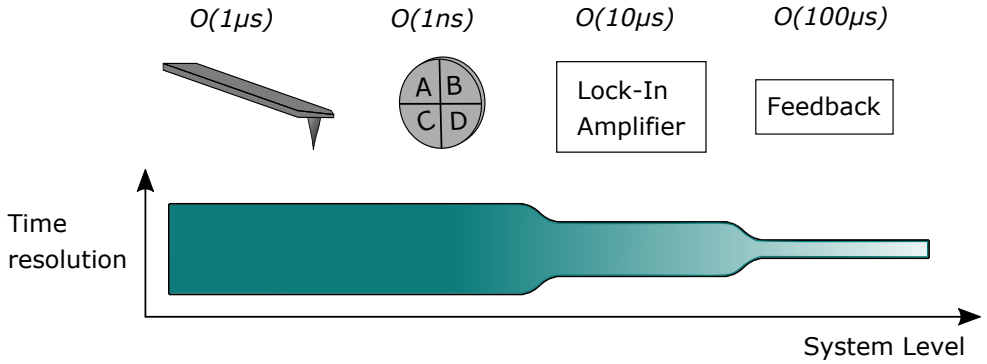

Figure 4.6.: Flowchart of temporal resolution in closed loop AFM setups. The scale indicates where bottlenecks are where temporal resolution is lost

Next, the cantilever oscillation is tracked by the position sensitive photo diode. Typical high speed semiconductor photo diodes on the market have response times of 1 ns second and below. This means that we can assume no temporal information is lost.
For all dynamic closed loop methods (where the feedback acts on the signal it gets

as an input) we need additional lock-in amplifiers. Their minimal measurable time is limited to their bandwidth. For modern LIA the upper limit bandwidth is in the MHz range suggesting a temporal resolution similar to the minimal temporal resolution. LIA work however most effective when their bandwidth is close to the signal bandwidth. Increasing the LIA bandwidth leads to additional intake of noise rendering higher bandwidths unpractical. Under real conditions, there is always noise present, which results in temporal resolutions of $\geq 1\mu$s at this point.
The last step in the signal chains are the feedbacks. To measure short changes high gains must be set, which in turn leads to unstable signal tracking. These Instabilities manifest themselves in additional noise. Hence we again have to make a trade off between temporal resolution and high SNR and due to the additional noise we can expect a decrease of the temporal resolution.
The limiting factors for closed loop AFM setups are thus the LIA and the feedback and temporal resolutions are between milli- and microseconds. Avoiding these two components and directly measuring the cantilever motion would decrease this resolution and several ansatzes exist for that. Collins et al. proposed such a method, where they digitise the signal from the photo diode and through post processing reconstruct the CPD computationally [70, 71]. This completely avoids the need for a LIA and a feedback loop. The temporal resolution is then only restricted by the cantilever and the photo diode.

Part II.

Experiments & Discussion

5. Methods

5.1. Cross Section Preparation

Due to their manufacturing procedure the investigated solar cells both have the same layout where the individual layers are deposited on a glass base substrate. Thus the top layer is the opaque cathode (usually gold). This makes it difficult to get a look inside the solar cell with an AFM as the top cathode is the only layer which can be directly accessed by the AFM tip. To circumvent this problem Bergmann et al. have developed a procedure where the cell is broken along the electrode and then irradiated with a focused beam of high energy gallium ions (short focused ion beam or **FIB**) [5] (see fig.5.1). With this technique they get nanometre flat cross sections of the cell.

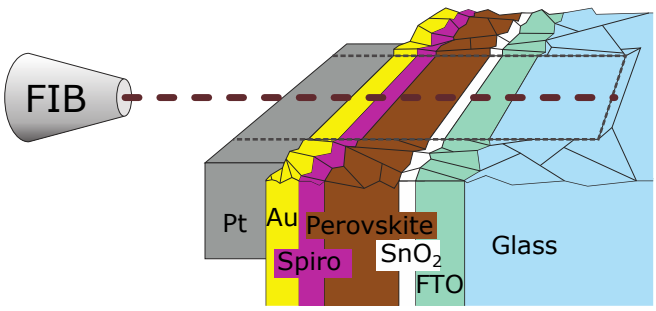

Figure 5.1: Cross section preparation of a planar PSC with the focused ion beam method. A 2μm thick Pt layer is deposited on top of the cell as a protection layer. The focused ion beam then polishes a flat surface into the cross section via sputtering.

Although yielding reproducible and qualitative results, this FIB method has a few drawbacks. For once milling times grow disproportional if one wants to investigate larger areas, with milling processes taking more than a few days to produce a cross section of 50 $\times$ 6 μm^2. This represents only a small excerpt of an otherwise macroscopic cell and poses a statistical limitation.
Additionally, the role of the gallium ions used in the ion beam is unclear. The Ga^+ ions are speculated to alter the crystal structure [72], such as incorporating defects and doping parts of the cell. As is known, doping a semiconductor leads to different properties, like a modified band structure, as compared to an intrinsic semiconductor. Bergmann et al. argued against that and showed no apparent signs of Ga contamination in the produced PSC cross sections [5] leaving yet room for further investigations.

In this thesis we introduce an advanced version for the preparation of solar cell cross sections. Here we use a Hitachi IM4000 ion milling system (short **Hitachi**). This device allows milling of larger areas within hours, thus decreasing the time it takes to prepare a cross section. The second mentionable improvement comes from the fact

that argon ions are used for milling. Argon is a noble gas and thus less reactive than gallium. We can thereby assume argon ions have a lesser impact on the cells regarding incorporation of ions into the materials.
For the cross section preparation we break the solar cell along one of its electrodes similar to the method by Bergmann et al. The polishing step is then performed with the Hitachi device. This device is specifically suited for milling cross sections of samples and has a sample holder for this purpose which includes a Ti mask to protect the sample from unwanted ion bombardment. The ions for the sputtering process come from an argon beam of 2-4mm diameter. A scheme is shown in fig.5.2 and an image of the cross section holder is shown in fig.B.1

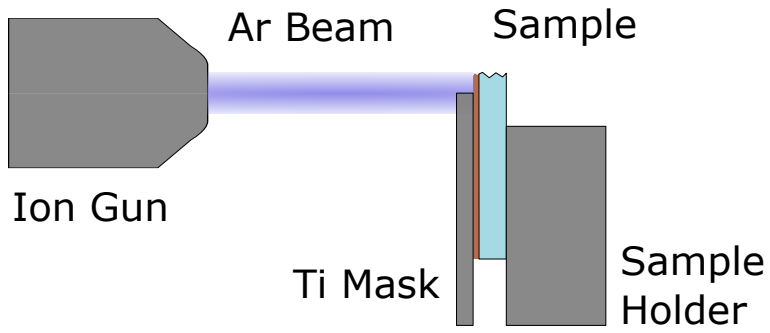

Figure 5.2: Scheme of the Hitachi cross section milling setup. The broken edge is milled away until it is flush with the Ti mask

To begin a milling process the mask and sample have to be aligned. For this, the sample is set to protrude a little bit above the mask (around 50-100μm) to expose a defined region to the argon ion beam (see fig.5.2). This protruding bit is milled away by the beam. The mask is a Ti plate piece with highly polished flat edges. Besides protecting the covered part of the sample from irradiation, the sharp edges of the mask yield highly flat cross sections by throwing a sharp defined shadow. In some instances (later described in sec.7) an additional thin glass slide of 100μm thickness is put between mask and sample. The reason is to decrease heating of samples by the argon ion beam.
Other parameters to optimise are the acceleration voltage for the argon ions which are ejected from an argon plasma. Typical values are 2 - 3kV. Additionally, the sample can be tilted while milling to give more ideal angles for higher sputtering yields, as well as avoid unevenly irradiating the cross section.

5.2. AFM and KPFM

All AFM measurements were performed with an Asylum MFP 3D AFM. Cantilevers used were Bruker SCM-PIT-V2 which have a n-doped (antimony) Si base that is coated with an PtIr alloy to allow for electrical measurements. The nominal first eigenmode of these cantilevers is at 75kHz. Test wise a stiffer Budget Sensors Electri-Tap 300-G with first eigenmode at 300kHz was also used.
For KPFM measurements a Zurich instruments HF2 lock-in amplifier was used (short **Zurich**). It includes a PLL and a PID feedback. Heterodyne FM KPFM is imple-

mented by combining the MFP 3D controller with the Zurich. For this, the MFP 3D sends two signals to the Zurich: the deflection of the cantilever and the drive signal with which the cantilever is excited. The drive signal is used as a reference to generate the ac bias for KPFM at $\omega_1 - \omega_0$. The deflection signal is sent to the PLL which constantly tracks the momentary resonance frequency $\tilde{\omega}_0$ of the cantilever. To get the amplitude of the oscillation according to eq.4.15 the Zurich LIA gets the deflection of the cantilever as input and is referenced to the frequency $\omega_1 - \tilde{\omega}_0$. To nullify this amplitude the Zurich PID feedback sends the dc bias for eq.(4.15) to the MFP 3D which applies it to the cantilever.
To avoid degradation of samples during AFM measurements, the AFM setup is placed in a sealed glove box, which is flushed with dry nitrogen.

5.3. Time-Resolved KPFM

In this thesis we use the time resolved KPFM method developed by Weber et al. [1]. Here the area of interest is mapped via a grid of pixels. At each pixel the cantilever approaches the sample surface and dwells there for a set time. During this dwell, experiments can be conducted like applying. A scheme is shown in fig.5.3. Collecting the data from all dwells gives a map of the processes taking place across the pixelated area of interest. The data acquisition for these maps is performed through one of the Zurich inputs. The Zurich has a sampling rate of 1MHz which is higher than the 2kHz from the MFP 3D controller previously used. Thus, by using the Zurich for the data aquisition we have access to the full temporal resolution which we estimate in sec.6.

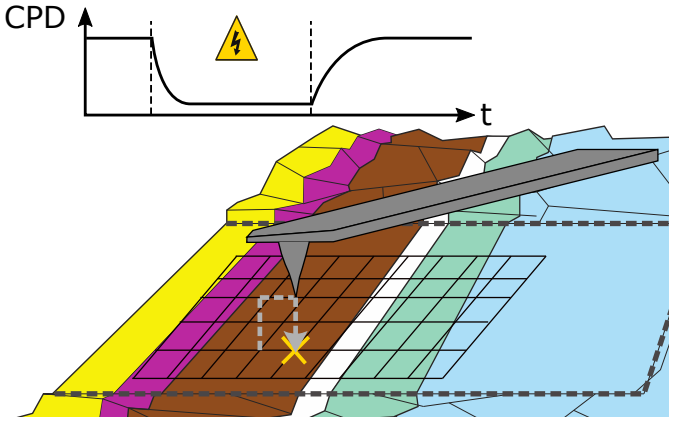

Figure 5.3: Scheme for a time-resolved KPFM measurement. The cantilever scans the surface in a pixel grid and dwells above the surface at each pixel. The graph shows the CPD measured and the reaction to an applied during the dwell. Image taken from [1] and modified.

6. Time Resolution of trKPFM

As mentioned in sec.4.4 the temporal resolution of KPFM depends, apart from noise, on the LIA and the feedback that calculates and applies U_{dc}. The aim of this chapter is to evaluate the temporal resolution of the KPFM system used in this work. Key role play the Zurich instruments lock-in amplifier and PID feedback (short **PID**) used, whose limits were explored. For this we measured KPFM on conductive highly oriented pyrolitic graphite (HOPG) and applied square wave signals $U_{sq,f}$ of different frequencies to it. Ideally the KPFM signal follows the square wave (with a system dependent potential offset). Due to the temporal resolution we can expect that there will be a rise time after which the KPFM output matches the discrete steps of the square wave. This rise time is the fastest possible reaction the KPFM setup makes and thus corresponds to the temporal resolution.

To start, we looked at the **error signal** U_{err} of the turned off PID. This signal is the output of the LIA that tracks the cantilever oscillation at $\omega_1 \pm \omega_0$ and thus is proportional to the uncompensated amplitude of the force according to eq.(4.15):

$$U_{err} \sim (U_{dc} - U_{CPD}) \tag{6.1}$$

Since it is also dependent on external applied biases, it responds to the square wave $U_{sq,f}$ we apply. By looking how fast this response is, we can estimate the temporal resolution of our LIA. The measurements were performed with a Keysight oscilloscope and example measurements are shown in fig.6.1. For the LIA measurements we used a f =100Hz square wave which switches from low 0V to high 1V.

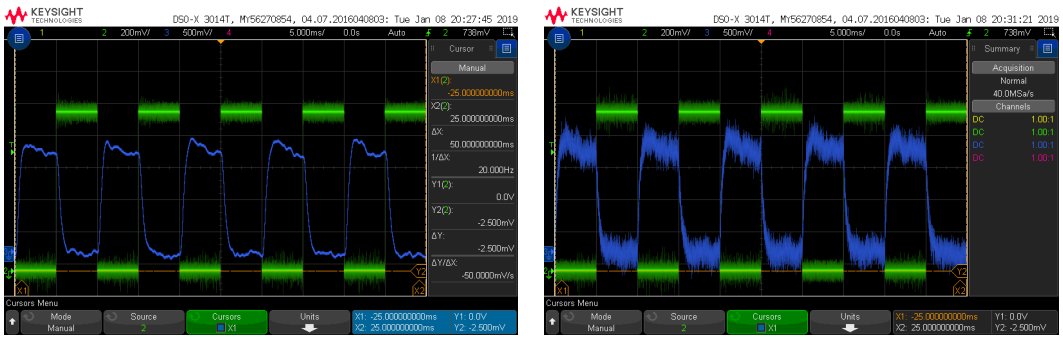

Figure 6.1.: KPFM error signal(blue) which responds to a square wave(green) analysed with an oscilloscope. Compared were LIA bandwidths from 1kHz to 50kHZ. The maximum and minimum explored bandwidths are shown.

As expected, the error signal changes in time with the square wave with a delayed exponential like slope. We thus use an exponential model to fit to the data according to:

$$U_{err}(t - t_0) = N \cdot \exp(-\frac{(t - t_0)}{\tau}) + c$$

This gives a time constant τ with which we can estimate the temporal resolution. We fit this model to each half period, meaning t_0 will be shifting together with the amplitude N that alternates its sign. An example of such a fit is shown in fig.6.2.

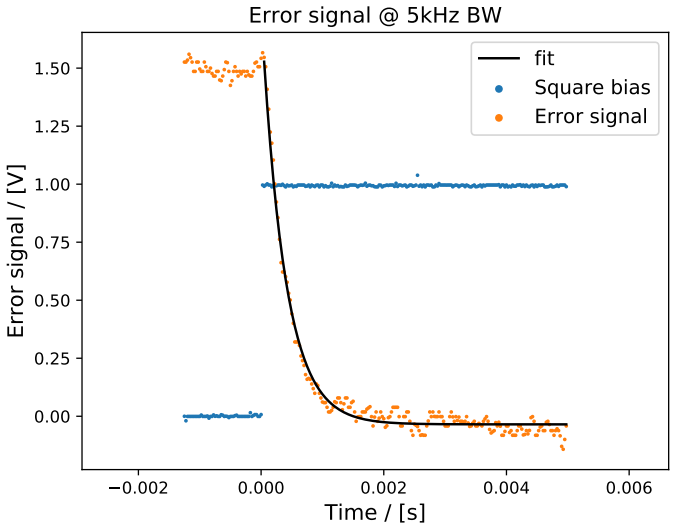

Figure 6.2: Uncompensated error signal for a LIA bandwidth of 5kHz and an exponential fit to it. Zero seconds mark the change from low to high voltage bias of the square wave

To get a statistically more significant value we average over at least ten half periods. The results for τ together with the noise level are shown in fig.6.3 and table B.1. The noise level is calculated as the standard deviation from the data at the flat tails of the exponential curves.

As the bandwidth increases, the time constant of the exponential response decreases while noise simultaneously grows. This is in line with the notion that higher bandwidths let faster responses pass. At the same time, a higher bandwidth accepts a wider frequency range of noise leading to an overall increased noise level. A saturation for the measured time constants can be seen and there is almost no change from 20kHz to 50 kHz. Thus, we measure a minimal temporal resolution from the LIA output of $\approx 310\mu$s. Striking is that the time constants are not inversely proportional to the bandwidth as one could expect from $\tau \sim \frac{1}{BW}$. For such a relation the time constant should be on the order of $\mathcal{O}(10\mu\text{s})$ for bandwidth $\mathcal{O}(10\text{kHz})$.

The error for the time constants was calculated from the standard deviation of all fits and is with $\approx 20\%$ high. This is a consequence of the single responses deviating from each other and the error we get from the single fits is an order smaller ($\mathcal{O}(1\mu\text{s})$). The error thus represents the heterogeneity of the error signal which gives an uncertainty to a single measured time constant.

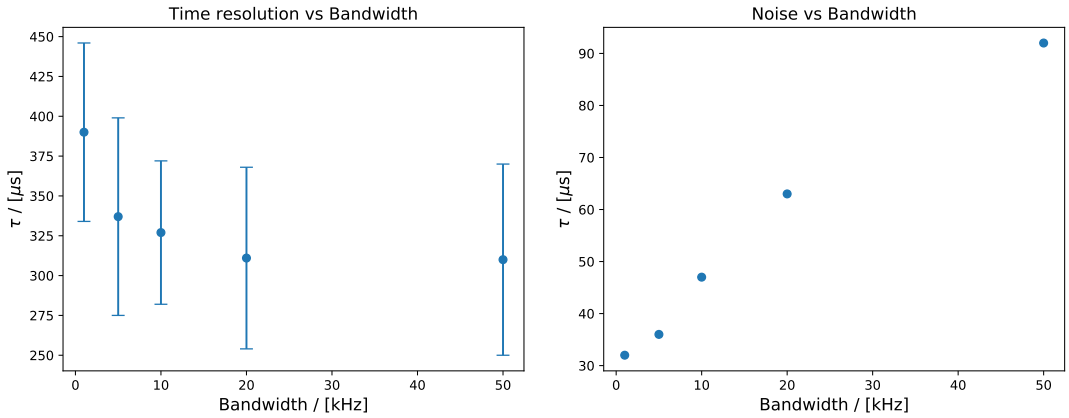

Figure 6.3.: Rise times (left) and noise level (right) of the error signal plotted against the LIA bandwidth. The rise time goes into saturation while the noise increases with higher bandwidths.

Next we turned on the PID and measured its control output. This is the KPFM signal corresponding to the system inherent voltage U_{sys} which is a combination of the CPD and the applied square wave: $U_{sys}(t) = U_{sq,f}(t) + U_{CPD}$. An example measurement is shown in fig.6.4.

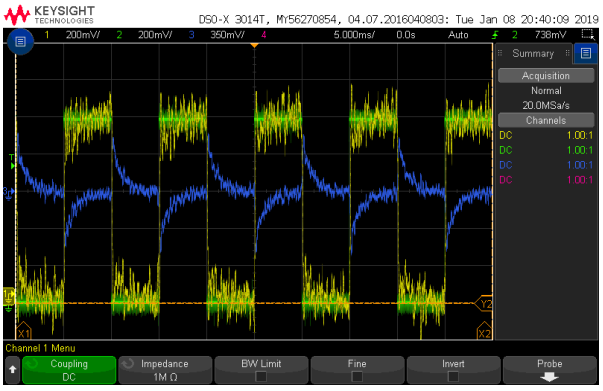

Figure 6.4: Measurement of the KPFM response to a square wave (green). The KPFM signal (yellow) matches the applied square wave. The error signal (blue) spikes at each change of the square wave as the PID has no time to compensate U_{sys}, until it falls to zero at the end of a half period

We see that indeed, the KPFM signal almost matches the square wave signal with the exception of a delayed response and increased noise. In the same manner as above, we fitted an exponential to the slopes to calculate time constants for the rise times. We did this for several frequencies f of the square wave to test the aptitude of three different PID settings for processes on different time scales. The PID settings were manually optimised to best reflect the square wave at frequencies 1Hz (**slow** setting), 100Hz (**standard** setting) and 1kHz (**fast** setting). Best means here a compromise between accurate tracking of the square wave with minimal noise. The LIA bandwidth was set to 5kHz for the slow and standard PID settings and 15kHz for the fast PID settings. To calculate the noise level, we took the KPFM signal from a 1Hz square

wave and calculated the standard deviation for a low and high voltage period from which we took the average. The results of the fits and the noise levels are shown in tables 6.1 and B.2. Again, the obtained time constants are an average of at least ten half periods and the error is the standard deviation.

	slow PID	standard PID	fast PID
Time constant τ / [μs]	406 $\pm$ 31	81 $\pm$ 17	35 $\pm$ 14
Noise level / [mV]	12	88	209

Table 6.1.: Mean rise times and noise level of the KPFM signal for different PID settings

We see a decrease of the time constants τ when optimising PID settings for higher frequencies f, indicating in fact higher temporal resolutions. Contradictory it seems that for 'faster' PID settings the rise times even undercut those of the error signal above by an order of magnitude (compare tables B.1 and B.2). This would mean that faster PID settings extract information from the LIA that is not there.
For faster PID settings not only a higher bandwidth was set but also higher P and I gains. These higher gains cause stronger reactions to shorter error signal changes, which can lead to overshooting. Indeed it is more probable that the tested two faster PID settings are dominated by overshoots caused by excessive gains. This is the more apparent when the uncompensated error signal is compared with the PID output for the same LIA bandwidth (see fig.6.5). For slow PID settings the PID output almost overlaps with the error signal. For faster PID settings the PID output jumps ahead of the error signal with an overshoot after which it returns to the same base level.

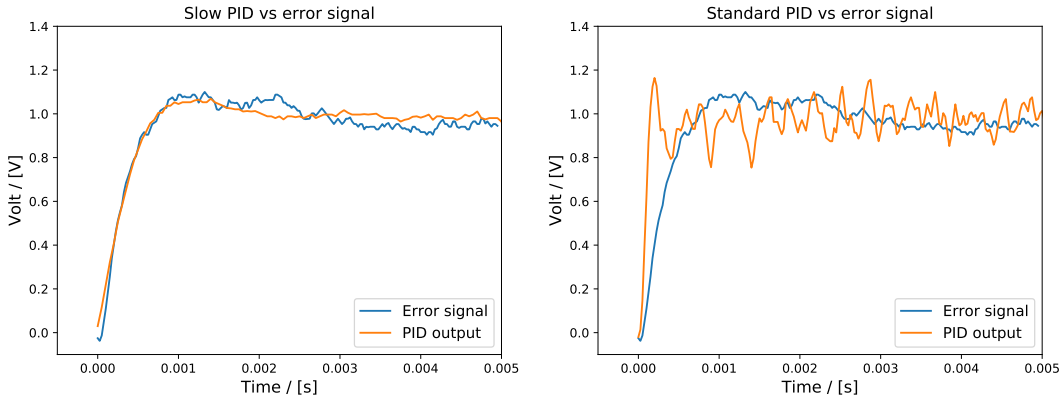

Figure 6.5.: Error signal (blue) compared with two PID settings (orange) at the same LIA bandwidth of 5kHz. The error signal was normalised to the same base level as the PID output for better comparison.

The exaggerated response of the faster PID settings to the voltage steps thus falsely suggest temporal resolutions below 100μs. The noise level increases for faster settings

for the same reason: the PID reacts abrupt to short fluctuations due to noise and thus amplifies them (see table 6.1). While it can be beneficial to have small overshoots, as this means a faster response to signals, it is often unwanted because it alters the real signal and leads to increased noise.
We can conclude that the temporal resolution measured with the slowest PID settings is the true one. The measured rise time here is on the same order as the ones obtained from the error signal above and overlap within the error. We can thus see that the PID retrieves the full information from the error signal, not reducing the temporal resolution.

To sum up, for closed loop KPFM methods it is necessary to tune the feedback system to the timescales that are in question. The way one does this is to turn up the bandwidth and PID gains as far as possible until the noise level increases without additional decrease of the temporal resolution. The minimal temporal resolution we can achieve with our setup is around $\approx 300\mu$s with a noise level of around 10mV. The limitation lies in the rise time of the error signal. We can point out that this limitation does not come from the LIA used, neither from the noise level present. With increasing LIA bandwidth the rise times of the error signal go into a saturation. A bandwidth of 50kHz would correspond to a minimal measurable rise time of around 20μs instead of 300μs. Thus, further investigation of the possible sources for the observed limitation is necessary. One source could be capacitive elements in our setup that increase the rise time according to $\tau = RC$.
With this in mind, we expect to be able to see charge dynamics from slow processes in the milli- to submilli-range for our PSC experiments.

7. Milling of samples

In the following, we will characterise and optimise the cross section preparation via the Hitachi device presented in sec.5.1. We look at three aspects: the quality of produced cross sections,the impact this method has on samples and how this impact can be reduced. We then try to compare FIB made cross sections with ones from the Hitachi device.
To explore the cross section preparation method we use two approaches. In the first approach, we use the Hitachi as is with only the Ti mask as protection. In a second approach we add a thin glass slide between mask and sample.

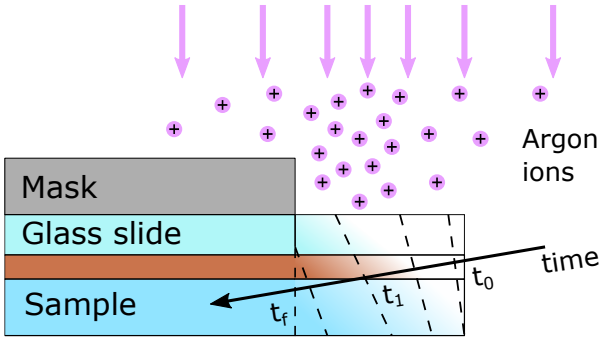

Figure 7.1: Progress of milling. Initially only the edge is significantly milled at t_0. After a time t_1 a slope appears and the bulk is milled away. Finally at t_f the mask blocks further the milling. The glass slide protects the sample from perpendicularly incident ions

The reason is to have an additional "custom" mask that continuously exposes more of the sample while it is being milled away itself. Since the milling advances from the sample edge onto the mask edge (see fig.7.1) a major portion of the sample is exposed to the perpendicularly incident beam for a prolonged time. This kind of sputtering is not efficient and leads to increased heating of the sample. The glass slide takes up this heat and spreads it more evenly avoiding local overheating.
A top view of a finished cross section is shown in fig.7.2. Visible is the imprint the beam profile left on the sample in the shape of a Gaussian function. In between the Ti mask and the sample, the glass slide used in this case can be seen. From its thickness of 100μm, the cross section width can be estimated to be around a millimetre wide. We thus see the advantage of getting large cross section areas within hours.

7.1. Thermal Impact of Milling

As described in sec.2.4, a side effect of sputtering is the thermalisation of a majority of the ions energy. Indeed, compared to the nA ion currents used in FIB milling the Hitachi shoots with ion currents of μA which could lead to previously not seen heat intake leading to melting. We therefore investigated the thermal impact the milling

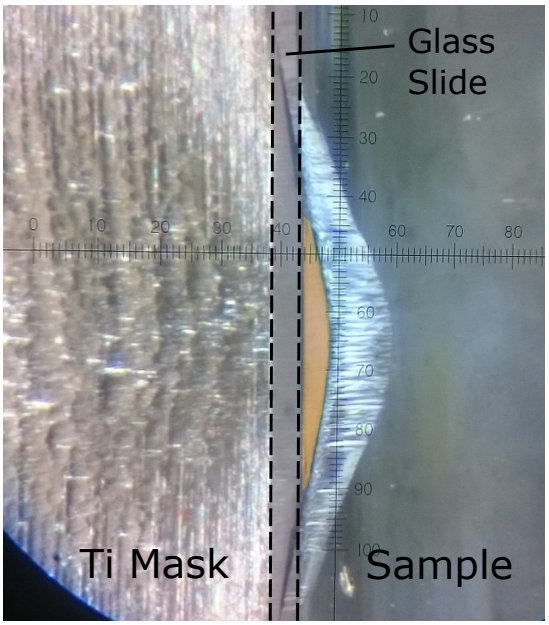

Figure 7.2: Result of a milling process as viewed from the top. To the left is the mask which also suffered wear. A glass protection plate is visible as a thin layer inbetween mask and sample. The orange highlighted area is flat and suitable for AFM measurements

process has on samples by milling a polyethylene glycol (PEG 8400) sample. PEG 8400 has a melting point of 52°C. The PEG film was deposited from a water solution through spin coating and the resulting thin film is heterogeneous with a bubbly structure. Assuming that when heated above its melting temperature the PEG film will change its form towards a more homogeneous equilibrium, we can estimate a bound for the heating during milling. We therefore took images with a scanning electron microscope (**SEM**) of the sample before and after milling for comparison (see fig.B.2).

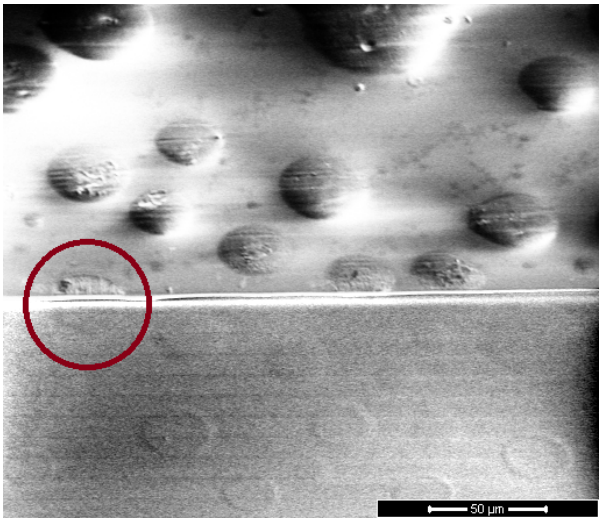

Figure 7.3: The lower half exposed to the ion beam is separated by a sharp line. Red marked is a bubble where half of it was exposed and the other protected. The original SEM image was edited (software GIMP) so that the lower half shows clearer contrast.

In a first run we only used the Ti mask as protection for milling. After milling, the exposed area has been sputtered away and shows only traces of the previous PEG

film. On a close look we can identify bubbles that were partially protected by the mask (see fig.7.3). Beside a smoothening through the milling process there are no evident signs that PEG melted and the film structure stayed the same.
We do however see signs of melting when we include the glass slide while milling. To compare both we milled a PEG sample where we covered half of the sample with a glass slide while milling. The milling time was short enough to not pierce through the glass slide. The results are shown in fig.7.4. We can see that the uncovered left side shows similar features as above: the majority of the film structure is milled away and far from the beam centre (indicated by the purple dashed circle) milling progress is slower. The right half shows no signs of abrasion as it was covered during milling. However, inside the beam centre (purple dashed circle) we see a structural change of the film which extends a bit into the area that was covered by the Ti mask.

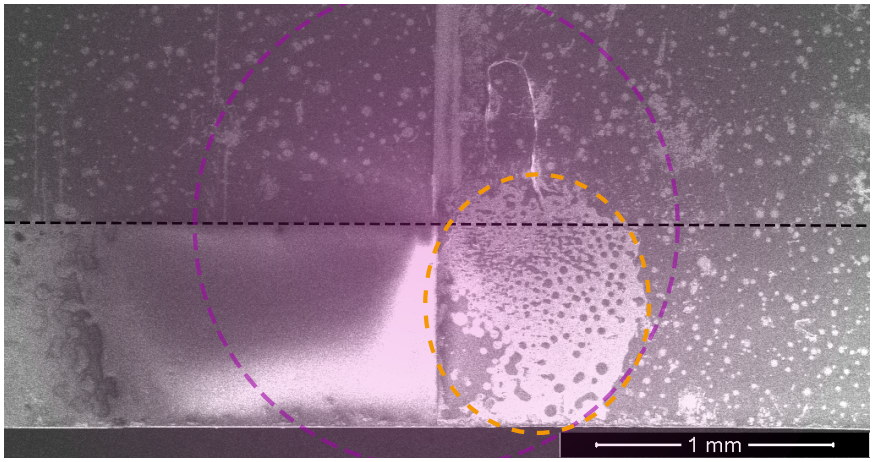

Figure 7.4.: PEG film after milling where the right side was covered with a glass slide. The PEG film is dark with brighter holes in it. The purple shade indicates the beam profile and the dashed circle shows the diameter of the ion gun exit. The region that shows signs of melting is highlighted with an orange dashed ellipses. The black dashed line shows where the mask was. The original image and the sample before milling are shown in B.3 and B.4

We assume the reason is that, indeed, we have excessive energy transfer to the glass slide which leads to heating. The glass slide then conducts this heat to the sample which is heated above the melting point of the PEG. This is especially true near the beam centre and we see less to no change outside of the ion gun diameter (purple dashed circle) as the beam intensity decreases here rapidly.

In the following we will make an estimation of the temperature thin films covered by the glass slide reach after a while of milling. We assume that after a while we have an equilibrium state where heating power $\frac{dQ}{dt}$ provided by the argon ions is conducted through the glass slide and sample into the sample holder. The sample holder represents a thermal reservoir of constant temperature T_0 (set to be room temperature

$T_0 = 23°\text{C}$). When we assume the total power of the beam is concentrated inside the ion gun diameter (purple dashed circle), the PEG region that melted takes up a quarter. When we further assume the material through which the heat is conducted is homogeneous glass we can use the stationary heat equation

$$\frac{dQ}{dt} = -\lambda A \frac{dT(x)}{dx} \qquad \Big| dt \tag{7.1}$$

$$T(x) = -\frac{x}{\lambda A}\frac{dQ}{dt} + c \tag{7.2}$$

to estimate the temperature at the position x. In this case λ is the thermal conductivity of glass ($\lambda = 0.8\frac{\text{W}}{\text{Km}}$), A a quarter of the area of the circle with diameter 1mm and c a constant given by the initial conditions we need to set when we integrate eq.(7.1). We can estimate the heating power to be the acceleration voltage of the argon ions times the ion current divided by four: $\frac{dQ}{dt} = U \cdot I = 3\text{kV} \cdot 60\mu\text{A}/4$. With the glass slide and glass substrate thicknesses of 0.1mm and 1mm ($\Delta x = 1.1\text{mm}$) we get for c

$$c = T(\Delta x) + \frac{x}{\lambda A}\frac{dQ}{dt} = 101.8°\text{C} \tag{7.3}$$

Putting everything into eq.(7.2) we get the temperature at the position of the PEG film as a rough approximation to be $T(x = 0.1\text{mm}) = 94.6°\text{C}$. This is indeed higher than the melting point of PEG (52°C) and explains the sings of melting we see in the beam centre. The thin film nature of the PEG film might lead to the PEG being milled away before the sample heats up to its melting point, hence showing no signs of melting at the unprotected side.
For the above approximation to hold it has to be guaranteed that the glass slide and the sample are in firm contact, meaning there are no gaps between the two. Keeping the Ti mask, glass slide and the sample in firm contact has an additional advantage: The heat introduced to the sample can better be conducted to the cross section holder.

What we can conclude from these experiments is that the sample can heat up in the beam centre up to $\approx 100°\text{C}$. This is still lower than the manufacturing temperatures of PSCs, meaning it is unlikely that our PSCs will take damage from overheating. As an optimal procedure for milling we propose a method where we adjust the sample with an offset to the beam centre. In that way the sample is positioned at the low intensity region of the beam profile and we can mill with lower effective beam currents while maintaining the same ion energies. The energy flux through the sample is thus reduced and heat build up is reduced. Furthermore when using the glass slide we propose adding thermal paste between the mask and the glass slide. In this way we achieve further 'decoupling' of the glass slide and the sample. Heat from the glass slide is then conducted to the cross section holder (through the mask) rather than to the sample.

7.2. Comparing Milling Methods

To explore which of the cross section preparation devices gives higher quality cross sections we tested both and compared results. For this we took two mesoporous PSCs: For the first we only milled a cross section with the Hitachi. In a second cell we milled a cross section first with the Hitachi and then on top of that with the FIB. The resulting cross sections of the cells are shown in fig.7.5.

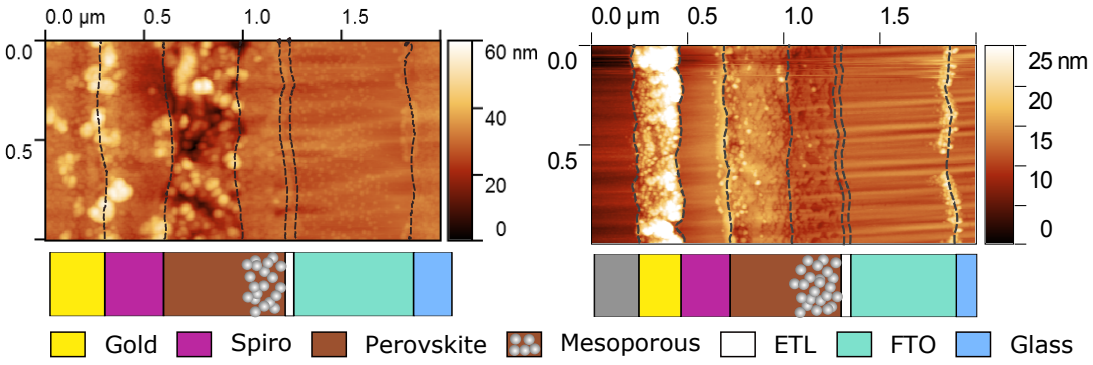

Figure 7.5.: AFM topography images of milled PSC cross sections. Left a cross section from the Hitachi, right from the FIB. For better layer contrast see the amplitude images B.5

Both methods produce surfaces with the same order of roughness. The FIB yields a smoother cross section with a roughness of ≈16nm compared to the Hitachi with ≈30nm. Both methods also show the layered structure of the cell, more pronounced in the FIB cross section though. By comparing the topography, amplitude and phase images obtained with AFM we can identify each layer by their contrasts. Helpful for this was a pre-estimation from the collaboration group at the EPFL which provided the cells used in this thesis. As an identifying feature, the bulk and mesoporous perovskite layers show the granular structure from the crystallisation of the perovskite. On top of the perovskite (left side) are the HTL, which for our cells is **Spiro**, followed by the gold electrode. For the FIB method there is also an additional Pt layer deposited on top. Beneath the perovskite are the TiO_2 ETL, followed by the fluorine doped tin oxide (**FTO**) electrode and the glass base substrate. The identified layers are marked in fig.7.5 and precise architectures with layer thicknesses are summarised in sec.A.1.
The ≈20-30nm thick metal oxide ETL is not actually visible. Its position is rather determined to be at the interface between the mesoporous perovskite and the FTO electrode. This uncertainty raises the question what the lateral resolution for our AFM experiments is? The lateral resolution is a result of the convolution of tip and sample topography. It is thus on the order of the tip apex radius which for the cantilevers we use is around 25nm. Although each layer can be distinguished distinctively there are no discrete transition points. The layers rather merge into each other. Additionally, the interfaces are not perfectly parallel. The error for an interface (position) is thus

higher, around 50nm.
A striking feature, that is more or less pronounced in all measured PSC cross sections is an additional layer at the FTO-glass interface. The substrates bought for manufacturing PSCs are typically glass with a transparent electrode on it. The additional layer we see could be adhesives used to guarantee that the transparent electrode sticks to the glass.
A difference between the two methods is how well layers can be distinguished. In the Hitachi made cross sections the layers are often only diffuse distinguishable. Compared to that, in the FIB cross sections each layer is distinctively recognisable. This can be explained with the focused nature of the FIB. The FIB sputters away material only very selectively which gives the prepared cross sections their flat topography. With the topography being rougher the fine lines at the interfaces are harder to identify. This is however not to say that good cross sections are not possible with the Hitachi. A last cross section we made, where the layers can be distinguished equally well is shown in fig.B.6.

As a conclusion, milling with the Hitachi can be used to quickly get cross sections that give a good overview of the cell architecture. The cross sections are comparable in quality to the ones from the FIB. The FIB however produces flatter cross section. As of now, the FIB method produces high quality cross sections more reliable. The same can however be achieved with the Hitachi with further optimisation, as can be seen from fig.B.6.
We yet have not addressed differences in the cross sections that could stem from doping of the cells. This will be done in sec.8.2.

8. Dynamics of Perovskite Solar Cells

In this part of the thesis we will combine the preparatory work from the previous two chapters to compare different PSCs by preparing cross sections of them and investigating the charge carrier dynamics with time resolved KPFM. We will look at two architectures: a cell with a mesoporous ETL that shows almost no hysteresis and a cell with a planar ETL that shows strong hysteresis. First we will describe the two cell cross sections and their architectures. We then investigate the potential dynamics in both cells under the influence of an external bias. According to sec. 3.2 hysteresis is predominantly caused by ion migration in the perovskite and its adjacent layers. We thus expect different behaviours with more pronounced slow dynamics for the planar cell than the mesoporous cell due to their different hysteresis magnitudes. Furthermore we will investigate the impact of the milling method on the cross sections.

To make sure the cells were still working and kept their respective hysteretic behaviour throughout the experiments we recorded J-V curves of the PSCs every time the cells where manipulated (i.e broken in half, milled, after measuring). Besides small losses and fluctuations in the efficiencies, the J-V curves showed no significant changes and hysteretic behaviour persisted (see table B.3, fig.B.9 and fig.B.10). For the mesoporous cell the mean measured efficiencies were 20.1±0.2% for forward curves and 20.2±0.1% for reverse curves. They show little to no hysteresis within the error (error taken as the standard deviation of at least 4 curves). The planar cell had mean efficiencies of 5.7±0.9% for forward curves and 10.2±0.9% for reverse curves. With this, the planar cell shows a J-V curve hysteresis with ≈50% difference between efficiencies measured in forward and reverse. We indeed reproduce the findings that mesoporous cells show less hysteresis than planar cells with elsewise similar layers[32].

After breaking the cells we polished them with the Hitachi device according to the steps in sec.5.1 and sec.7, using the variant with the added glass slide for better distribution of heat. The resulting cross sections are shown in fig.8.1.
We can again identify the single layers from the topography, phase and amplitude signals. This is however not so easy for the mesoporous cell. Here are signs of a 'double tip' visible. When a cantilever tip gets damaged or picks up dirt, two apexes can occur. Both of these apexes then contribute to topography imaging which leads to a loss in lateral resolution by a duplication of features. However we see a clear layer contrast in the CPD measured with KPFM (see fig.B.8). Thus, we additionally used the CPD to identify the layers for the mesoporous cell.

In the course of the past year that lead up to this thesis, continuous improvements

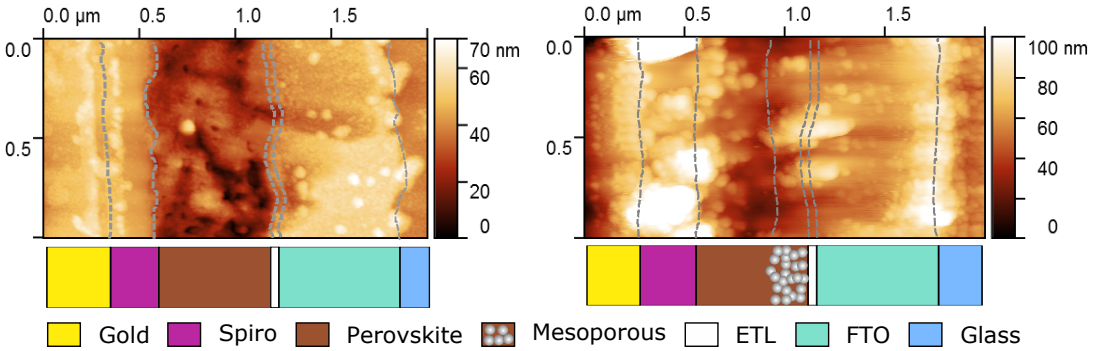

Figure 8.1.: Cross sections of the two investigated PSC architectures prepared with the Hitachi (left planar, right mesoporous). The dashed lines separate layers that were identified according to the colour scheme from fig.3.1. For original images see appendix B.3

were made not only to the cross section preparation but also to the KPFM settings used for the time resolved experiments. This means that the measurements on the mesoporous PSC, which were made close to the end yielded much more significant results. The measurements of the planar cells in contrast were made at an earlier stage. Since the KPFM data here shows stronger noise due to PID settings being not fully optimised, results from this cell can only be discussed qualitatively.
In the next chapters we compare the dynamic responses of both PSCs when a bias voltage is applied. Additionally, we give a quantitative analysis of the dynamics in the mesoporous cell. We then compare the results on a qualitative basis with the dynamics in the planar cell.

8.1. Planar vs Mesoporous PSC

To investigate the mechanisms behind J-V hysteresis, we compared time-resolved KPFM data of a mesoporous PSC (short **meso cell**) cross section with a planar one. These architectures exhibit different degrees of hysteresis[32].
As discussed in sec.2.3, the CPD depends on the work function which in turn depends on the local Fermi energy. This is evident when we combine eqs.(2.5) and (2.6):

$$U_{CPD}(x) = \frac{E_{f,sample}(x) - E_{f,tip}}{e} \tag{8.1}$$

With KPFM we measure these local differences in the Fermi energies. A schematic that explains the relation between work functions, Fermi energy alignment and the local CPD was given by Hermes et al. [73] and is shown in fig.A.4.
The CPD distributions across the cell show the work functions of the layers after the alignment of the Fermi energies. The **static CPD distributions**, in the absence of any disturbances, are shown for both PSC cross sections shown in fig.8.2. The position of the single layers are visualised by the background colours. We obtained all

curves by averaging over at least 20 scan lines to reduce noise. There were no severe differences between the scan lines used for averaging, thus justifying this step.

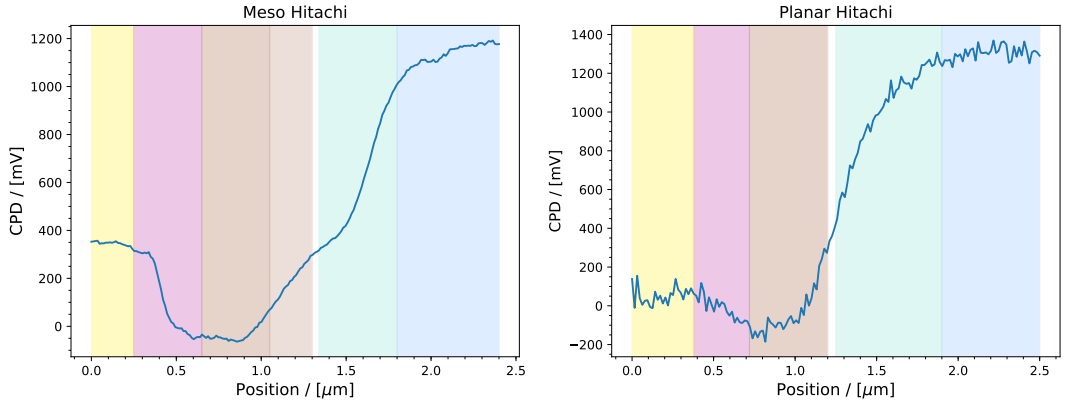

Figure 8.2.: Static CPD for both cell architectures. A general downwards trend from bottom to top electrode is visible. Both architectures show a potential well centred at the S-P interface.

We can see in both cross sections a similar CPD trend: A downwards slope from the glass substrate to the top gold electrode with a local minimum near the Spiro-Perovskite interface (short **S-P interface**). In the meso cell the minimum is around 400mV lower with respect to the gold layer, whereas it is around 300mV in the planar cell. A reason for the potential difference at SP-interface for both cells could be changes in work functions due to surface contaminations or different perovskite doping levels. A stronger n-doping of the perovskite layer can increase its potential relative to the electrodes.

To investigate the dynamic behaviour of the PSCs we take a look at the CPD response after applying a voltage pulse to the cells. For this we applied negative bias pulses of -0.6V and 500ms duration to the bottom FTO electrode while the gold electrode was grounded. Prior to this bias the cell is in an equilibrium state. Here, perovskite solar cells are decribed as p-i-n junctions, with an intrinsic perovskite layer surrounded by charge selective contacts, that together generate a built-in electric field across the junction. Since perovskite is assumed to be a mixed electronic/ionic conductor due to low formation energies for mobile ions and vacancies, mobile ions would distribute along the build-in field and screen it (compare fig.3.4). When we apply a bias we introduce an additional electric field that drives the cell out of its equilibrium. We expect that there are intermediate potential states that show the redistribution of mobile ions, when turning the bias on and off.

In the next chapter we will discuss these dynamics quantitatively for the mesoporous cell. Due to the noise present in the measurements made on the planar cell we will

compare both cells qualitatively.

8.1.1. Short Circuit Bias On

To better visualise the dynamic processes we subtract the static CPD distribution from the subsequent potential curves. In this way we get the relative change in potential and can focus on the processes happening inside the cell upon application of a bias. The relative potentials of the meso cell at different times after turning on the bias are shown in fig.8.3

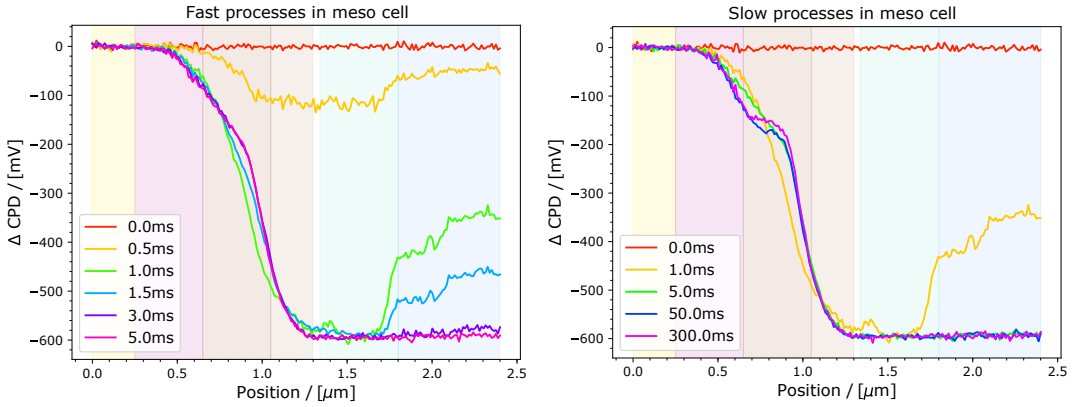

Figure 8.3.: Relative potential across the meso cell at different times after turning on the bias voltage (at zero seconds). During the first ≈1-2ms the bias builds up at the FTO (left). During the remaining time of the pulse a new equilibrium develops (right)

Before applying the bias at zero seconds, the relative potential ΔCPD is zero everywhere since we subtracted the static CPD. 2ms after applying the bias we can measure the full voltage difference of -0.6V between the grounded gold and the FTO electrode. The resulting potential gradient starts at the centre of the Spiro layer and goes to the mesoporous layer. However, in the region of the potential gradient we see more processes taking place. Here we observed an overshoot near the bulk-mesoporous perovskite interface (short **P-M interface**) to lower voltages. This overshoot relaxes within 5ms to an equilibrium gradient. After that, a potential step appears at around 50ms in the bulk perovskite near the S-P interface. This step is fully formed within 200ms and persists for the rest of the bias pulse (fig.8.3, right side). The final potential distribution is asymmetric and the gradient at the P-M interface is around four times higher than the one at the S-P interface.

The potential step can be interpreted as a shielding of the external applied field inside the bulk perovskite. The underlying processes can be explained when we assume a model of a mixed electronic/ionic conductor. The bias generates an electric field across the cell almost instantly. This field is strongest in those layers where the electric resistance is the highest. These are the perovskite and its surrounding charge

selective contacts since they are semiconductors. The mobile ions rearrange along this field until they reach an interface that acts as an obstruction. In this way the inside of the ionic conductor is partially shielded from the imposed field. Since the external field builds up faster than the ions can move, it takes 200ms before they can screen the field. Thus we have an overshoot from a yet uncompensated field.
However, in this model we can not explain the asymmetry in the gradient. We need further modification of the model concerning the role of the interfaces. It is probable that the interfaces to the contact layers are no barriers for the ions but are permeable. Weber et al. made propositions explaining this behaviour in planar PSC [1, 73]. They suggested that iodide ions move through Frenkel defects to the S-P interface due to the applied field. Here they form complexes with the Spiro. These iodide ions originate from a thin region near the P-M interface. The resulting ion distribution consists of a thin, positively charged area of iodide vacancies near the P-M interface and a diffuse, negative space charge of iodide ions that gets stronger towards the S-P interface, where they are bound to the Spiro. Even though this model was proposed for a planar cell architecture, it seems to explain our results on a meso cell.
Unclear is however why the positive charges in our meso cell accumulate at the P-M interface. Assuming that the bulk and mesoporous perovskite are ionic conductors we would expect the positive charges to form at interface of the mesoporous TiO_2 and the compact TiO_2 due to the external field. Thus further experiments are necessary to elucidate the role of the P-M interface.

Assuming that the mobile negative iodide ions form an electrostatic double layer at the interfaces we can fit an exponential decay to the relative potential to get the ion concentration according to:

$$\Delta CPD = N \exp\Big(-\frac{x - x_0}{\lambda_d}\Big) + c \qquad , \qquad \lambda_d = \sqrt{\frac{\varepsilon_r \varepsilon_0 k_B T}{2 c_0 e^2}} \tag{8.2}$$

Here λ_d is the Debye screening length, ε_r and ε_0 the relative and vacuum permittivities, respectively (as an approximation we used ε_r =60 for perovskite and TiO_2[1, 74]), k_B the Boltzmann constant, T room temperature and c_0 the ion concentration in question. The resulting fits are shown in fig.8.4. For the ion concentrations we get $c_{0,P} = (2.16 \pm 0.03) \times 10^{15} \frac{1}{\mathrm{cm}^3}$ in the bulk perovskite near the S-P interface and $c_{0,P-M} = (3.56 \pm 0.01) \times 10^{15} \frac{1}{\mathrm{cm}^3}$ at the P-M interface. Weber et al.[1] calculated values in the same order of magnitude. The differences in the concentrations could be explained by a complexation of negative iodide with positive Spiro dopants [73]. Since this only takes place at the S-P interface we have a higher concentration of negative iodide at the P-M interface.

To compare the both cells we made the same experiment with the planar cell and the resulting potential dynamics are shown in fig.8.5.
The planar cell shows a similar response as the meso cell: The potential at the FTO electrode drops to the applied voltage within 1ms and we see an overshoot of the potential gradient. Here the gradient initially stretches from the gold-spiro interface

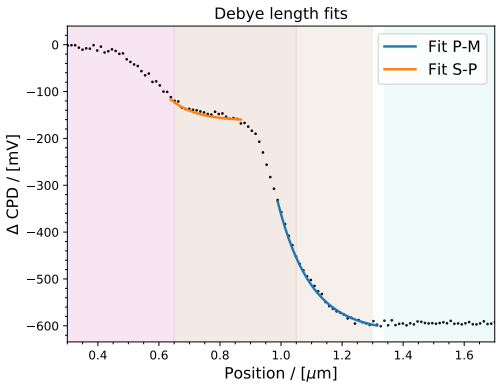

Figure 8.4: Electrostatic double layer model fitted to the potential at the end of the 500ms bias pulse, for the mesoporous cell. Shown is only an excerpt of the measured cross section from above.

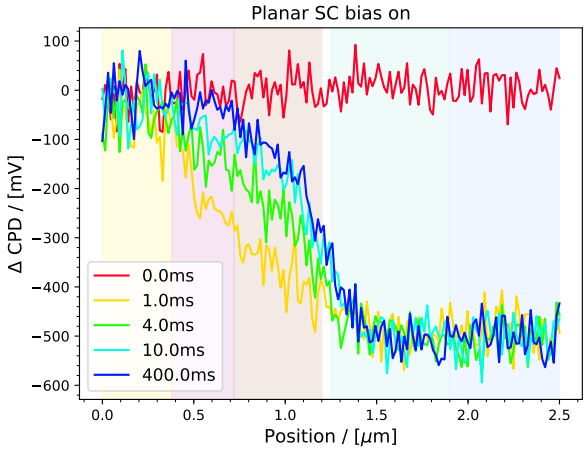

Figure 8.5: Relative potential across the planar cell at different times after turning on the bias voltage (at zero seconds). 1ms after turning on the bias we see an overshoot in the Spiro and perovskite layer that relaxes after 10ms.

to the FTO. After around 10ms the potential gradient relaxes to an equilibrium that persists for the rest of the bias. In this equilibrium state the gradient is mostly localised in the perovskite layer within the error of the lateral interface positions. We do not observe additional processes like the formation of a potential step. This however could be attributed to the presence of noise.
Surprisingly, the timescale for the planar cell to reach its equilibrium after bias application is an order of magnitude shorter than for the meso cell. Considering the magnitude of the hysteresis measured in both devices, this result contradicts our expectations, in which we should observe slower dynamics in the planar cell with its stronger hysteresis. However, Weber et al. showed in planar cells timescales of several hundred milliseconds for the potential gradient to relax. A possible explanation for this discrepancy could be that our planar cell experienced excessive heating from the Hitachi preparation method changing the cell. The amorphous structure of the planar cell cross section could show signs of melting (see fig.8.1).

The potential curves found 500ms after turning on the bias represent a new equi-

librium. When turning off the bias, the cells should from there relax back to their initial equilibrium. We can expect that the time scales for this relaxation reflect the processes that led to the new equilibrium in the first place.

8.1.2. Short Circuit Bias Off

Next we turned off the bias voltage and recorded the potential distribution during the relaxation back to the initial equilibrium. We display the dynamic changes during this relaxation via the relative potential as done above (results see fig.8.6 and 8.7).

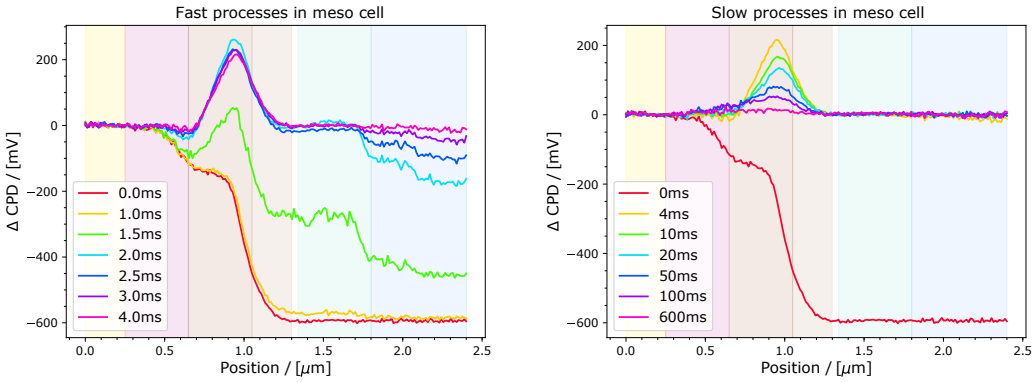

Figure 8.6.: Relative potential across the meso cell at different times after turning off the bias voltage (at zero seconds). During the first 2ms the relative potential returns back to zero at the FTO electrode. A positive potential overshoot appears in the bulk perovskite near the P-M interface (left). This positive potential overshoot persists for around 200ms (right).

The potential on the FTO electrode relaxes back to zero within a few milliseconds but overshoots to positive values in the bulk perovskite near the P-M interface. The overshoot is around 250mV high at its maximum and persists for ≈200ms.
Assuming localised charges are the reason for the measured slow processes we can use the Poisson equation to infer charge distributions from the potential for the 1-d case according to:

$$\rho(x) = \varepsilon_0 \varepsilon_r \frac{\partial}{\partial x} E(x) = -\varepsilon_0 \varepsilon_r \frac{\partial^2}{\partial x^2} \Phi(x) \tag{8.3}$$

We calculated such charge distributions after turning the bias on and off and the results are shown in secA.2. From the curvature of the potential it follows that the overshoot resembles positive charges that remain after the bias is turned off. These positive charges are accompanied by negative charges at both sides of the overshoot peak. As described above, the positive charges could represent iodide vacancies. The surplus of these vacancies persist for hundreds of milliseconds because their counterparts, the iodide ions, are bound to the Spiro and are only slowly released [1]. This behaviour was previously observed by Weber et al. on a planar cell architecture, where

the overshoot persisted for almost 500 ms [1]. Considering the stronger magnitude of hysteresis measured on the planar device by Weber et al. than the meso cell characterised here, we propose that the faster decay of the overshoot contributes to the lower hysteresis of the meso cell.

For the planar cell we measure a similarly strong potential overshoot of around 250mV that appears within 1ms after turning off the bias (see fig.8.7). This overshoot is spread across the perovskite layer and persists for around 4ms. With the different magnitudes

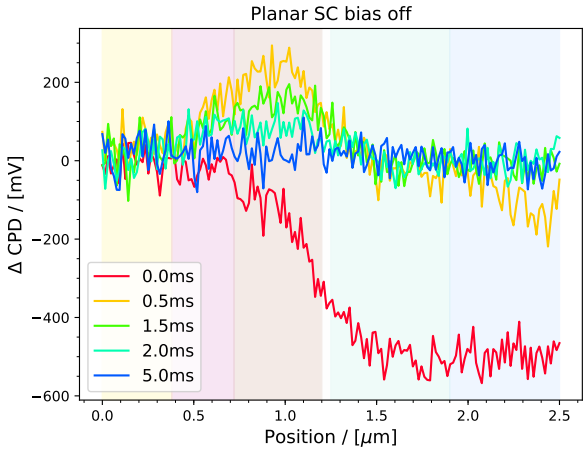

Figure 8.7: Relative potential across the planar cell after turning off the bias. A positive potential overshoot appears after ≈0.5ms that is spread across the perovskite layer. After 5ms this overshoot has decayed and no further changes occur.

of hysteresis detected for the planar and the meso cell, this result is again surprising. We would expect longer durations of the overshoot, comparable to the 500ms measured by Weber et al [1].

To summarise, we see processes in the mesoporous similar to those reported by Weber et al. for planar cells [1]. These can be interpreted as mobile iodide ions drifting to Spiro when a negative bias is applied to the FTO electrode. The iodide ions leave behind positively charged vacancies at the P-M interface and form charge neutral complexes at the S-P interface. When turning off the bias the iodide ions are only slowly released until the cell is in equilibrium again.
The lifetimes for the positive charges we observed in our meso cell are approx. twice times faster than those measured by Weber et al. in a planar cell. We can link this to the low degree of hysteresis present in meso cells as compared to higher degrees of hysteresis in planar cells. The lifetimes of the overshoot in the planar cell measured here, are unfortunately not reliable due local changes of the cell. These changes could be induced by excessive heating from the preparation method.

In the above discussion we focused on the potential changes across cell cross sections and gained insight on charge movements. In the next section we will further utilise the technique of time-resolved KPFM and look at the temporal details at single points for the mesoporous cell.

8.1.3. Detailed Potential Dynamics

The detailed processes happening in the mesoporous cell are more apparent when looking at the relative potential at a single position (or rather pixel). From sec.6 we found that the temporal resolution for our setup is around 300μs. Thus it should be possible to observe processes in the cells on this time scale. To reduce the noise, we took pixels of the same x-position from at least 20 scan lines of an image and averaged over them.
We start this discussion with the potential dynamics at the FTO electrode (see fig.8.8). Since FTO is an electric conductor the potential drops almost instantly to the applied bias. We can fit an exponential to the potential slopes and calculate rise times. From

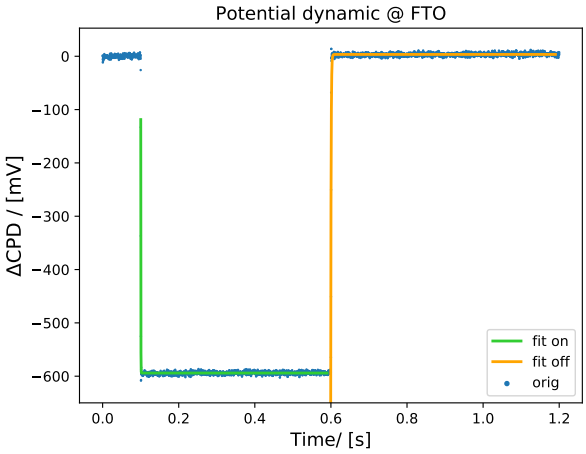

Figure 8.8: Potential dynamics at the FTO electrode for the mesoporous cell. Plotted are exponential fits to the potential slopes after turning the bias on and off.

the rise time of the potential drop we recognise the temporal resolution of our time-resolved KPFM setup to be around 300μs.

Next we investigate the layers where the ionic rearrangement processes take place. For the mesoporous cell this is the bulk perovskite layer. Here we first look at a position near the P-M interface where we saw a negative potential overshoot after turning on the bias. The results are shown in fig.8.9).
We can identify four processes (marked with Roman numerals) that are discernible after turning on the bias and that are visible across a distance of around 300nm in the bulk perovskite (compare fig.B.13). First there is a sharp drop due to the applied bias (**I**) followed by an equally sharp counter response (**II**). Next a slow recovery to lower potentials occurs (**III**) before the potential finally relaxes over the course of a few hundreds of milliseconds (**IV**). Such alternating transitions have not been described yet to our knowledge.
We suggest that step I and II correspond to a fast capacitive charging followed by an initially fast rearrangement of ions in the bulk perovskite that shield the external field. Step III and IV would correspond to delayed ionic responses. These could be a result of lower ion mobilities in the mesoporous perovskite for example, or a pile up of

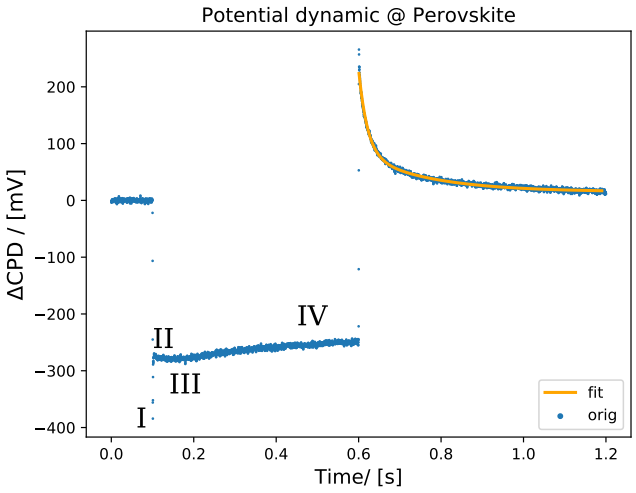

Figure 8.9: Potential dynamics in the perovskite layer of the Hitachi milled cell. Four different processes are identified with Roman numerals. A double exponential was fitted to the slow decay after turning off the bias

negative ions in the mesoporous layer at the P-M interface. Latter can be backed up by higher concentrations of negative ions at the P-M interface compared to the S-P interface (compare sec.8.1.1 and fig.8.4).

There are less features distinguishable after turning off the bias. We see the positive overshoot described in the section before as a sharp spike followed by a slow decay. We can model the slow processes via a decay reaction according to:

$$\frac{dN(t)}{dt} = \lambda N(t) \tag{8.4}$$

The solution of this equation is an exponential with a decay time $\tau = \frac{1}{\lambda}$. We can thus approximate the potential changes by a double exponential. This should represent a fast capacitative charging combined with a slow ionic rearrangement. We thus fit the following model to the potential curves:

$$\Delta\text{CPD}(t - t_0) = A \cdot \exp\left(-\frac{(t - t_0)}{\tau_1}\right) + B \cdot \exp\left(\frac{(t - t_0)}{\tau_2}\right) + c \tag{8.5}$$

The results for the time constants τ_i are shown in tables B.4 and B.5. We calculated the decay time for the neutralisation of the positive charges after turning the bias off to be ≈160ms. Weber et al. calculated faster decay times of around 125ms. However they used a single exponential fit which could have lead to faster decay times by combining the fast capacitive with the slow ionic component.

8.2. Milling Impact on Cells

In this section we continue the comparison of our meso cell cross sections prepared via the FIB method or the novel Hitachi method. While we only compared the topographical quality of the cross sections in sec.7, we now look at the CPD distributions

across the cell with KPFM. For this we take the mesoporous cell from sec.7 where we prepared a FIB cross section and a Hitachi one on the same cell.
The penetration depth of sputtering ions is on the order of few nanometre for the energies we use [75]. Since we mill a few micrometres into the Hitachi cross section with the FIB, we can expect no influence of the previous milling steps.
The cross sections in question are summarised in fig.8.10.

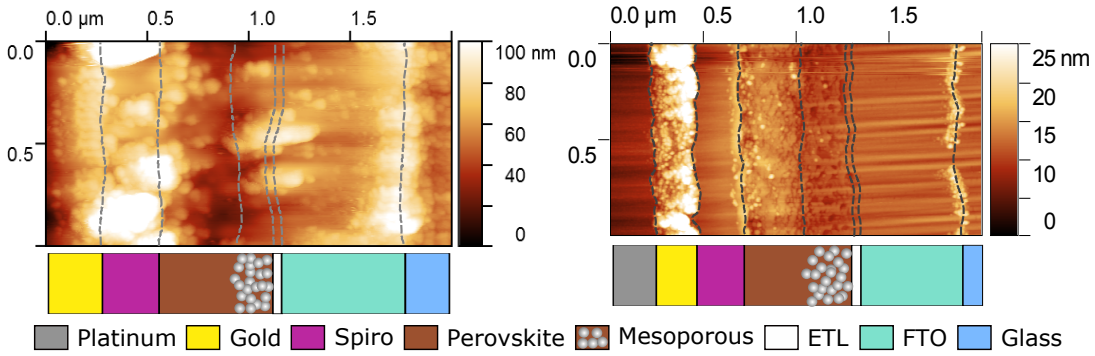

Figure 8.10.: Two cross sections of the same cell. The left one was prepared with the Hitachi the right one with the FIB

We discuss the same routine as in sec.8.1: we first compare the static CPD distributions (see fig.8.11) and then plot the relative potential change during the bias pulsing. As a CPD reference we can take the gold layers and the platinum layer for the FIB

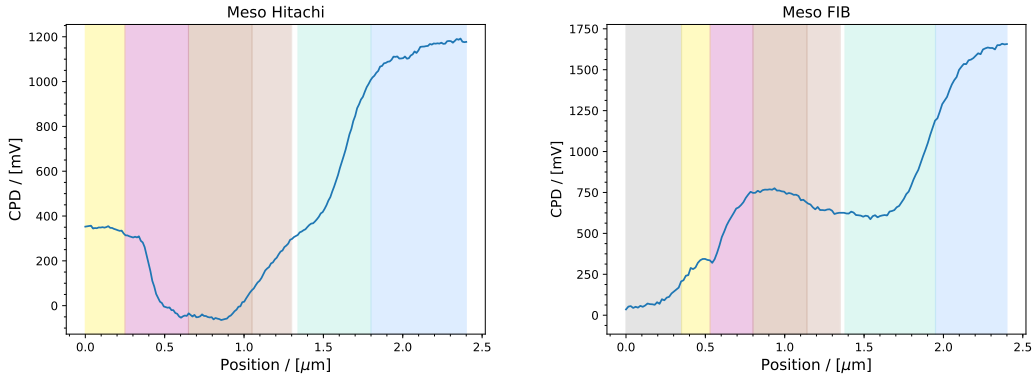

Figure 8.11.: Static cross section CPD for both milling methods. A general downwards trend from bottom to top electrode is visible. The Hitachi made cross section shows a potential well centred at the S-P interface while the FIB one has a local maximum here.

made cross section. Since the cantilevers we use have a platinum-iridium coating, the CPD should be around zero at the FIB platinum layer. Indeed, we see a CPD of approx. zero at the bulk of the platinum. At the gold layer we see approx. the same

CPD in both cross sections.
The Hitachi mesoporous cross section was already discussed in sec.8.1 so we will only describe differences with respect to the FIB cross section. The FIB cross section also shows a downwards trend of the CPD from the FTO to the gold layer. We see however a difference around the bulk perovskite layer. While we have a potential well in the Hitachi cross section in this layer, the FIB one shows a local maximum. The difference between the minimum of the potential well in the Hitachi cross section and the local maximum in the FIB one is around 700mV.

For a comparison of the dynamic responses in both prepared meso cell cross sections, we conducted the same bias experiment for the FIB mesoporous cross section. The comparison for the bias on part is shown in fig.8.12 and for the bias off part in fig.8.13. We see differences in the bias experiments between the cross sections from

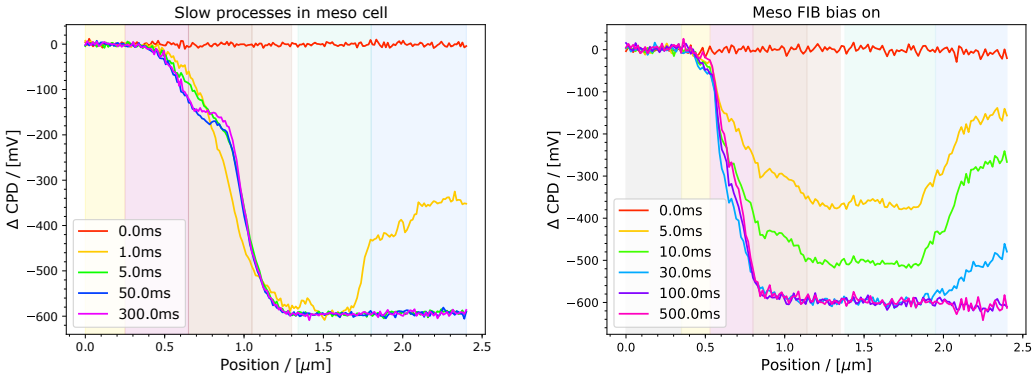

Figure 8.12.: Relative potential for both preparation methods after turning on the bias. The potential gradient shows differences between the Hitachi (left)

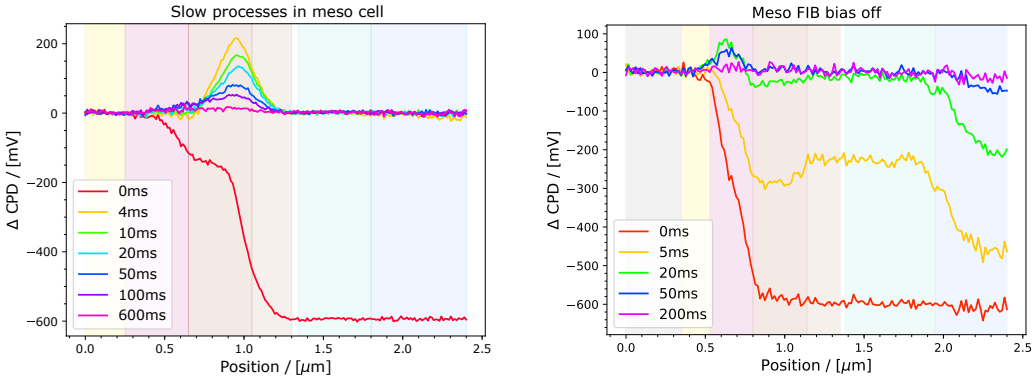

Figure 8.13.: Relative potential for both preparation methods after turning off the bias. The positive overshoot appears in the FIB cross section in the Spiro layer (right), while it appears in the bulk perovskite in the Hitachi one (left).

different preparation methods. While we also see the applied voltage difference between the gold and FTO electrode in the FIB cross section, the gradient inbetween the electrodes differs. The potential gradient is almost completely localised in the Spiro layer. This indicates that the Spiro layer has the largest resistance in this cross section. The FIB cross section shows a similar overshoot of the potential gradient as in the Hitachi cross section. Thus we observe a similar shielding of the external field in the Spiro layer. However, in the FIB cross section no potential step appears. Without such a step, the potential gradient stays symmetric after an equilibrium is reached. This takes around 100ms.
After turning off the bias, the relative potential relaxes back to zero and we see an overshoot. Compared to the Hitachi cross section, the overshoot is localised in the Spiro layer in the FIB cross section. This overshoot is 100mV high and persists for 100ms.

To sum up, we see slow processes in the FIB cross section. These slow processes occur in the Spiro layer. This is unexpected as we assumed ionic conductivity to be restricted to the perovskite layer. We analysed only excerpts of the cells of around $2\mu m^2$. It could be that for the FIB cross section we measured at a defective spot of the cell that shows a different doping, compared to the other cells presented in this thesis. The gold layers as references show approx. the same CPD. The shift in CPD at the S-P interface and at the perovskite, with respect to the gold, correspond to different levels of doping (compare fig.A.4). Here an advantage of the Hitachi method becomes apparent: since it yields larger cross section areas we can also measure over a larger area. This gives more statistical significance.
Another reason for the difference could be an unintended damaging of the perovskite when milling with gallium ions. Rothmann et al. reported that perovskite samples prepared for transmission electron microscopy with a FIB, do not represent the pristine perovskite [72]. However for their preparation method, they shot directly at the perovskite. In contrast, for our preparation method we have an additional platinum protection layer and shoot at almost flat angles. Furthermore we see similarities between the mesoporous cell prepared with the Hitachi method and the planar cells investigated by Weber et al. which were prepared with the FIB method.

To clarify the effect of the preparation method on PSC cross section further experiments have to be made. An approach would be preparing cross sections on the same sample with three preparation methods: First one where the cell is only broken without any ion irradiation. Second one with the Hitachi method and a third one with the FIB method. With this it should be clear if the milling procedures have an effect on the PSC and if so which preparation method affects the cells more.

9. Conclusion and Outlook

In this thesis, we aimed to optimise two fundamental experimental procedures for the visualization of carrier dynamics on the cross sections of PSCs via time-resolved KPFM: we investigated a novel ion milling approach for the preparation of smooth PSC cross sections. Furthermore, we characterised and improved the temporal resolution of our KPFM setup from 500 to $\approx 300\mu$s. Finally, we applied these experimental procedures to two PSCs with different architectures and degrees of hysteresis to compare their charge carrier dynamics.

To achieve the minimal time resolution of $\approx 300\mu$s, the settings for the LIA and the PID feedback have to be adjusted to the time scales in question. This is done by increasing the LIA bandwidth and the gains of the feedback until the KPFM signal becomes unstable due to noise. The resolution found is limited by the response rate of the error signal. The response rate in turn, is not inversely proportional to the LIA bandwidth as one might expect and goes into a saturation. Reason for the limited temporal resolution could be coupling of signals to the cantilever oscillation or hidden capacitive elements that increase the RC time of the system. Further investigations could identify the sources that lead to the resolution limitations.
The time resolution however can be pushed beyond the limits of a closed loopd KPFM setup. Collins and Ginger et al reported a post processing approach where the complete cantilever oscillation is recorded and digitised [70, 71, 76]. Through data analysis quantitative values for the CPD can be obtained. This method is only limited by the photodetector response time and ultimately by the resonance frequency of the cantilever. These limitations are on the order of micro- to nanoseconds.

For the novel solar cell cross section preparation method we utilised a Hitachi IM4000 milling device, that shoots with high energy argon ions. Early experiments with the Hitachi device showed that samples heat up due to energy intake from the argon beam. This is especially true in the beam centre. By using a glass slide as a heat absorbing cover and milling at the low intensity tail of the beam we minimised the thermal impact on samples. When the glass slide is adhered with thermal paste to the Ti mask, the conduction of heat from the glass slide to the sample will further be avoided. After this optimisation we showed that we can produce cross sections of PSCs with the Hitachi method. The prepared cross sections are comparable in quality to the ones prepared with the FIB, in that they yield nanometre flat surfaces where single layers are distinguishable.

We could show that we can make KPFM experiments on the cross sections fabricated

with the new preparation method. In these experiments we studied the response of two PSCs to an external bias, with the aim of:

1.) Comparing the dynamic behaviour of PSCs with different degrees of hysteresis.

2.) Comparing the impact of the milling on the dynamic behaviour of the cells.

For these comparisons we analysed several benchmarks of the cell cross sections, including the dynamic potential changes and charge distributions over time.
The results of our mesoporous cell show that similar processes are present as compared to the planar cell measured by Weber et al. [1]. These processes are governed by slow ionic rearrangements. We show that these processes occur faster in our mesoporous cells than in the planar cells reported by Weber et al. This difference could be one of the reasons that mesoporous cells show less hysteresis than planar ones.
Surprisingly, we found faster processes in the planar cell we measured. This could be attributed to the fact that the planar cell showed signs of melting and thus is not representative.

Moreover, we showed the presence of additional processes in the mesoporous cell that go beyond the model proposed by Weber et al.[1]. We did not find such processes in our planar cell yet, which raises the question if these processes are linked to the presence of hysteresis. However, we could have missed such processes due to the presence of noise in our planar cell measurements. Refined measurements with optimised KPFM settings should clarify if similar processes happen in both cell types.

We saw indications that the method used for preparing the cross sections influences the outcome of KPFM measurements, be it FIB or Hitachi. This could be from a yet not fully controllable milling process. An advantage of the Hitachi method over the FIB one is its ability to produce fast large scale cross section.
To determine which method is less invasive, more experiments have to be made. These could involve comparing cross sections milled with either method with an area on the same cell that did not experience any milling.

With this thesis, we further highlight the advantages of a fast time-resolved KPFM for locally measuring electrostatic dynamics.

A. Appendix

A.1. Cell architectures

For the PSCs investigated in this thesis the top electrode was gold. As a HTL 2,2',7,7'-Tetrakis[N,N-di(4-methoxyphenyl)amino]-9,9'-spirobifluorene (short **Spiro**) was used. For the perovskite absorber a high efficiency triple cation variant was used ($Cs_x(MA1-yFA_y)_{100-x}Pb(I_{1-z}Br_z)$). In the case of the mesoporous cells an additional perovskite percolated mesoporous TiO_2 layer is used which lacks in the planar cells. As ETL metal oxide layers were used; TiO_2 for the mesoporous cell and SnO_2 for the planar cell. As bottom electrodes both cells have fluorine doped TiO_2. The cells use glass as a substrate base. The layer thicknesses were measured by the collaboration group from the EPFL Lausanne via SEM images of PSC cross sections and are summarised in table A.1.

Mesoporous cell	Planar cell	layer thickness / [nm]
gold		100
Spiro		200
triple cat perovskite		500
mesoporous layer		150
TiO_2	SnO_2	15-30
FTO		500-1000
glass substrate		
total cell thickness		≈1500-2000

Table A.1.: Layer thicknesses of the PSCs investigated

A.2. Charge Distributions in Meso Cross Sections

To calculate charges in the mesoporous, Hitachi made cross section after turning the bias on and off we apply the Poisson equation to the relative potential according to:

$$\rho(x) = \varepsilon_0 \varepsilon_r \frac{\partial}{\partial x} E(x) = -\varepsilon_0 \varepsilon_r \frac{\partial^2}{\partial x^2} \Phi(x)$$

We implement the Poisson equation by first smoothening the relative potential curves via a Savitzky-Golay filter with polynomial order three and a filtering window of 25nm. We then numerically calculate the second derivative of the filtered potential to get the charge distribution. The filtering is necessary, to suppress charges that arise

from the second derivate in the noise. Although the charge distribution is dependent on the local relative permittivity we omitted any local dependence of ε_r and set it to one. The reason is that the permittivity is unknown close to the layer interfaces. Here we cannot assume homogeneous bulk materials and layer interactions change the local permittivity. However, since we only investigate the charge dynamics at a single position, we do not need information about ε_r. The calculated charge distributions are shwon in fig.A.1 Visible is the generation of two dipoles after turning on the bias:

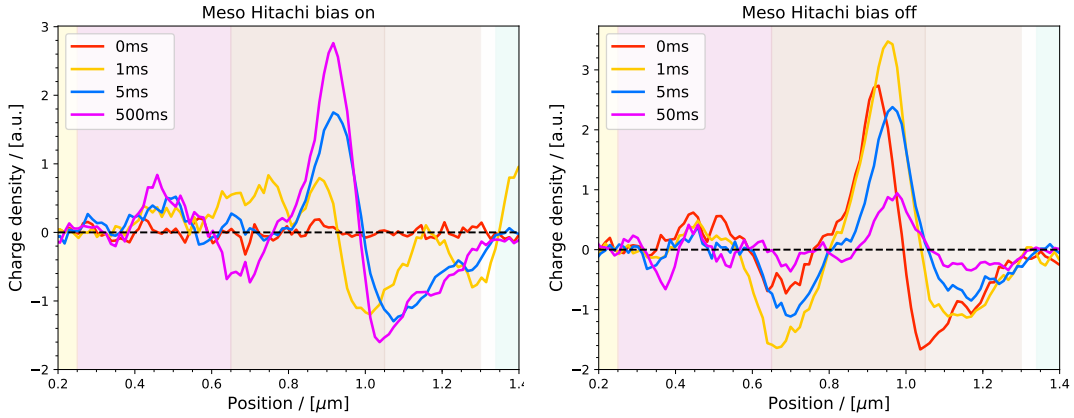

Figure A.1.: Charge distributions in the meso Hitachi cross section after turning the bias on (left) and off (right)

one large one at the P-M interface and a smaller one at the S-P interface. The small one can be identified as negative iodide ions that move to the Spiro layer. There the negative charges induce a positive polarisation in the Spiro. The larger dipole results from positive iodide vacancies in the bulk perovskite near the P-M interface. As mentioned in sec.8.1.3, the negative charges in the mesoporous layer could come from iodide ions that pile up at the P-M interface.
After turning off the bias these dipoles start to decay. The positive charges from iodide vacancies decay after around 200ms.

A.3. Schematics

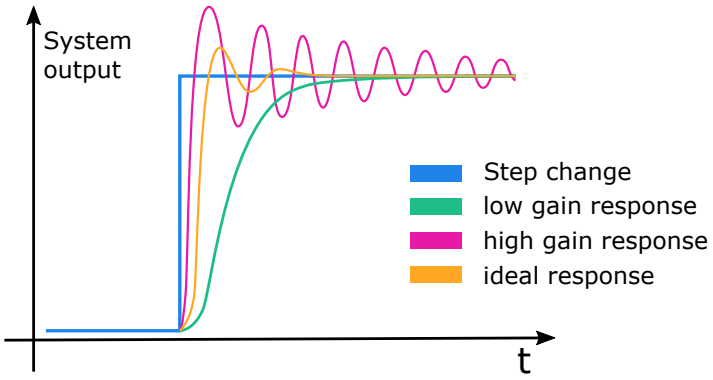

Figure A.2: PID responses to a step change for different gains. For low gains the PID response is insufficiently slow. For excessively high gains the PID can start to oscillate.

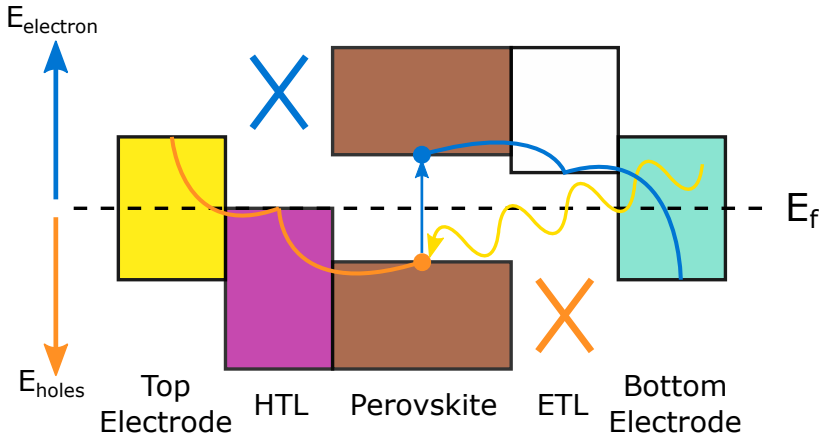

Figure A.3.: Schematic of the charge extraction in PSC. The coloured rectangles show the simplified band diagram near the Fermi energy when the layers are in contact. The electron (blue) is excited via a photon (yellow) to the conduction band and moves to lower energy states in the ETL and from there is quenched at the adjacent electrode. Since there are no close states energy states in the HTL, the excited electron is hindered in moving in this direction. The same applies to the hole left in the valence band (orange), except in the other direction.

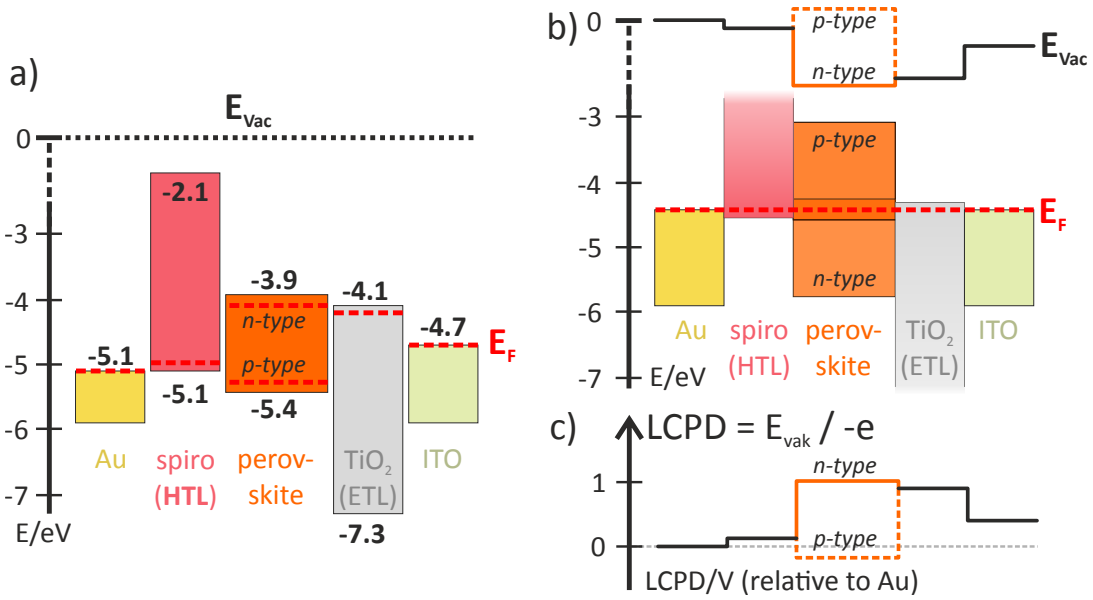

Figure A.4.: a) Fermi energies of the PSC constituents, considering different doping levels in the perovskite absorber. b) Fermi energy alignment in a PSC. c) The resulting CPD distribution as measured with KPFM. Since the CPD is defined with respect to a positive charge we have to take the negative.

B. Supplementary

B.1. Time Resolution of KPFM

Bandwidth / [kHz]	time constant τ / [μs]	Noise level / [mV]
1	390 ± 56	32
5	337 ± 62	36
10	327 ± 45	47
20	311 ± 57	63
50	310 ± 60	92

Table B.1: Results of the fits to the error signal for different LIA bandwidths

PID setting	Square Wave f / [Hz]	Time constant / [μs]
slow	100	282.9 ± 13.4
	250	330.8 ± 14.3
	500	605.5 ± 64.7
	1000	†
	1500	†
	2000	†
	mean	406.4 ± 30.8
standard	100	85.7 ± 14.5
	250	75.2 ± 12.0
	500	75.3 ± 16.1
	1000	80.5 ± 20.8
	1500	88.0 ± 19.5
	2000	†
	mean	81.0 ± 16.6
fast	100	‡
	250	‡
	500	31.7 ± 12.4
	1000	42.4 ± 17.8
	1500	30.8 ± 5.3
	2000	35.4 ± 14.2
	mean	35.1 ± 14.3

Table B.2.: Results of the fits to the KPFM signal. † means fits were omitted because the square wave changed too fast for the PID to follow. ‡ means the noise level was too high to make a fit to the data.

B.2. Milling of samples

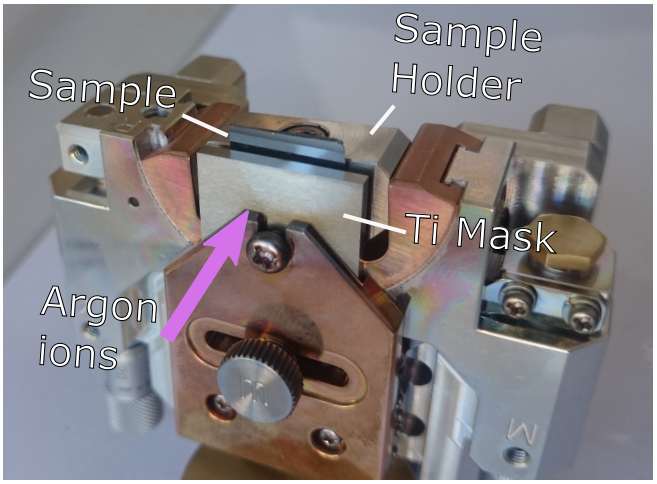

Figure B.1: Image of the Hitachi device cross section holder. The purple arrow indicates the direction from which the argon beam irradiates the sample. As an example sample a piece of silicon is shown.

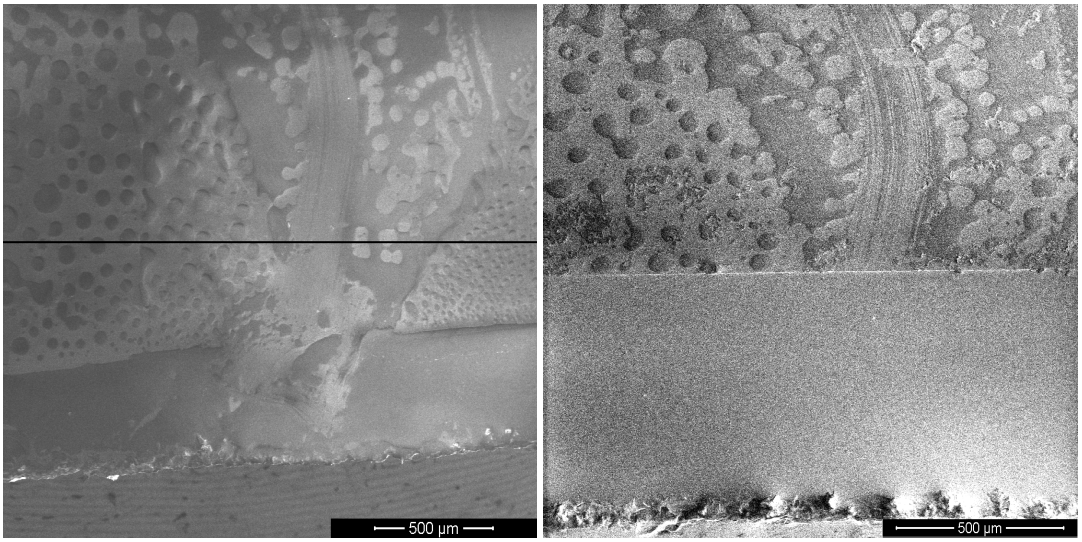

Figure B.2.: PEG sample before and after milling. The PEG film has a bubbly structure where the bubbles are holes in the PEG film. The black line indicates where the mask was positioned

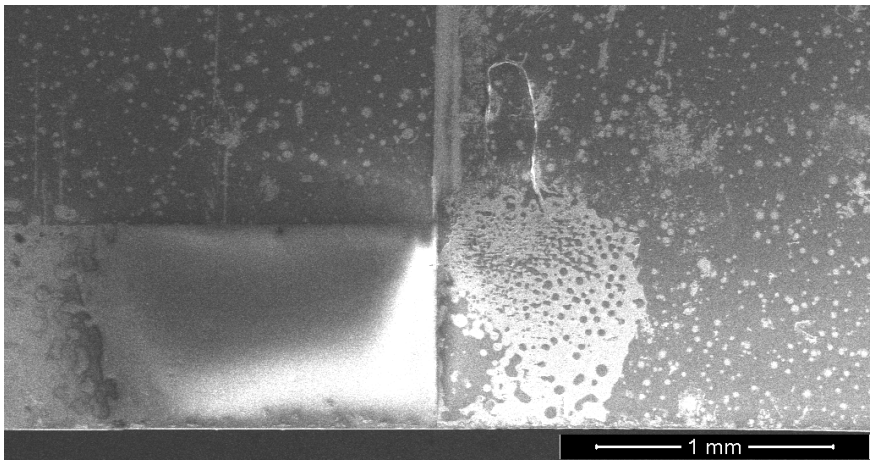

Figure B.3.: PEG film after milling where the right side was covered with a glass slide.

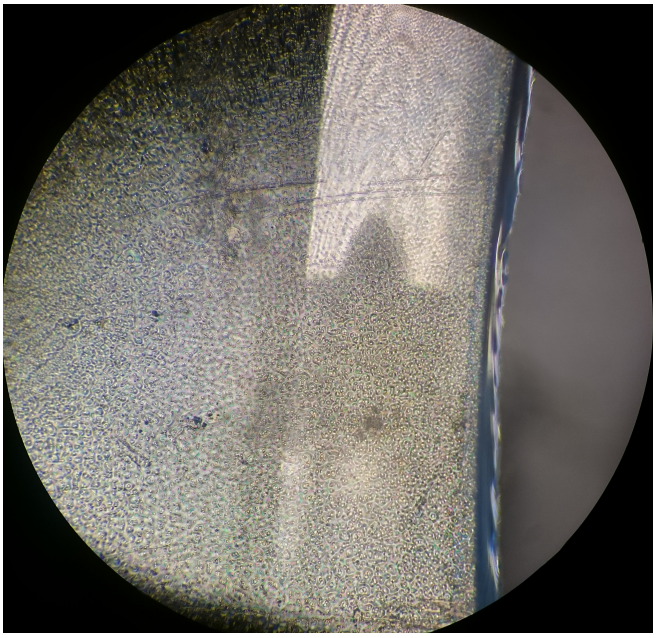

Figure B.4: PEG film for the glass slide comparison experiment before milling under an optical microscope

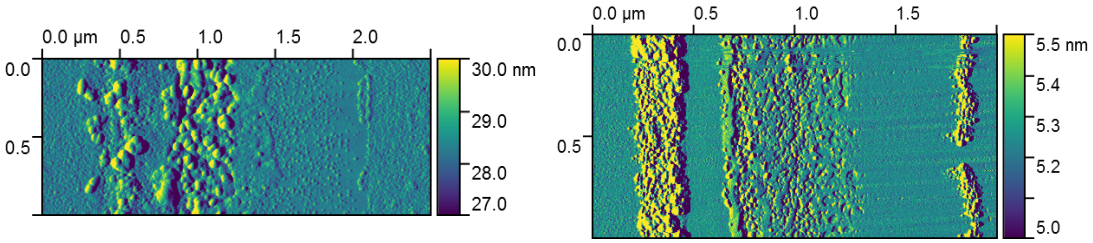

Figure B.5.: Images of the amplitude in dynamic AFM mode of milled PSC cross sections. Left a cross section from the Hitachi, right from the FIB.

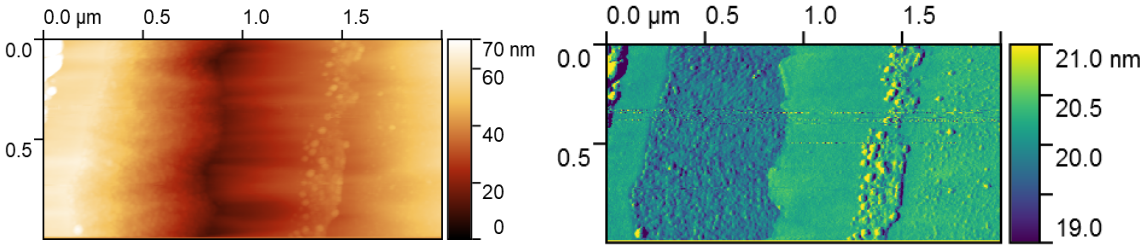

Figure B.6.: Cross section of a planar PSC made with the Hitachi. This was the best achieved cross section from the Hitachi. The amplitude image shows a clear and crisp contrast between the single layers.

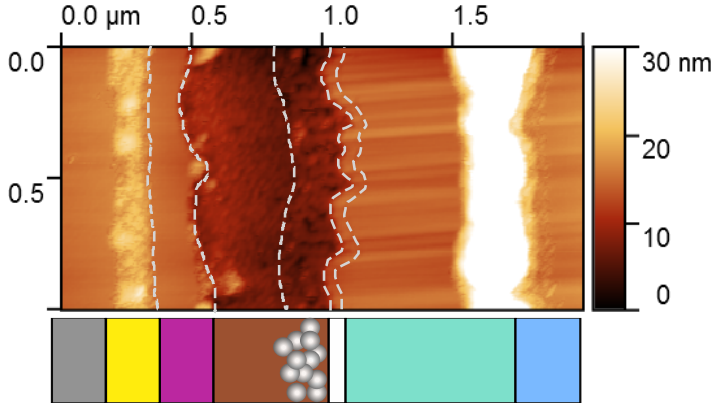

Figure B.7: Another FIB cross section of the meso PSC studied. Here the unknown material between at the FTO-glass interface is more pronounced

B.3. Dynamics of Perovskite Solar Cells

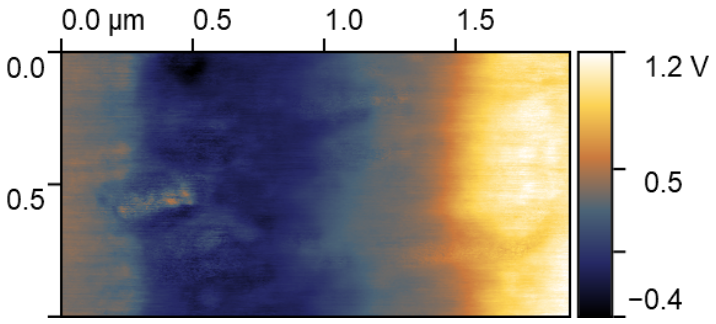

Figure B.8.: CPD image measured from the meso cell Hitachi cross section. Layers can be differentiated by contrasts in the CPD.

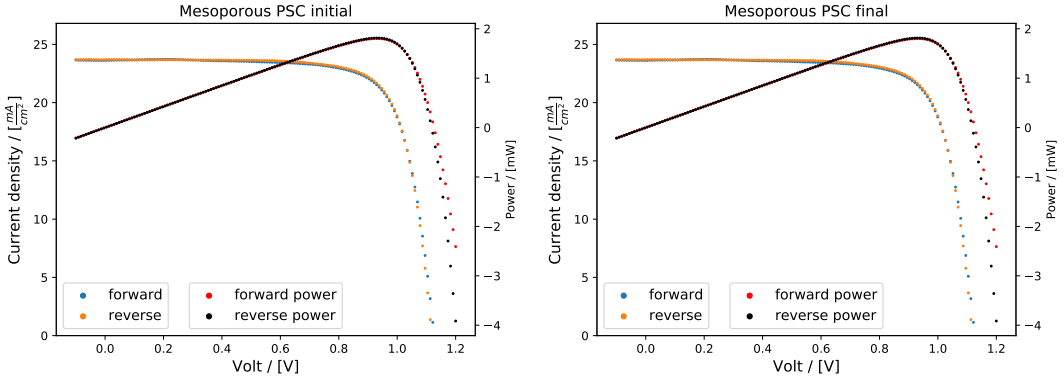

Figure B.9.: J-V curves of a mesoporous cell at the start (left) and end (right) of an experiment cycle

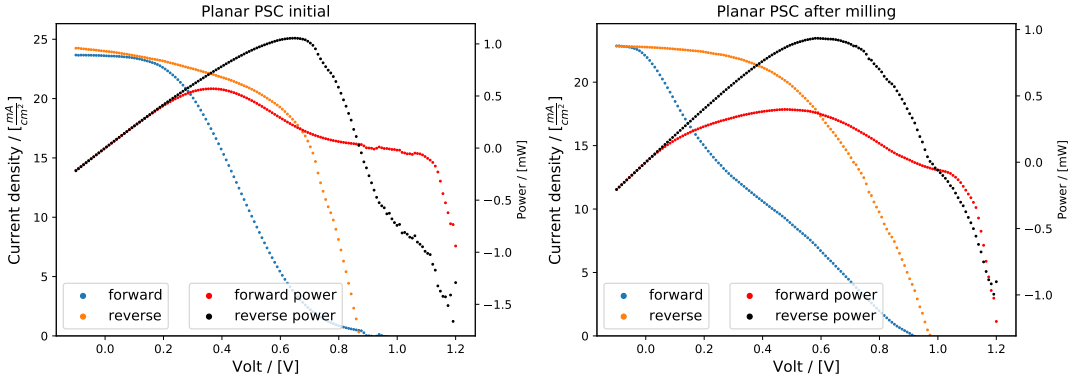

Figure B.10.: J-V curves of a planar cell at the start (left) and end (right) of an experiment cycle

	mesoporous / [%]		planar / [%]	
step	forward	reverse	forward	reverse
initial	20.1±0.1	20.1±0.1	7.0±0.8	10.5±1.1
after milling	20.2±0.1	20.1±0.1	5.2±0.9	9.6±0.6
final	20.0±0.5	20.5±0.1	5.0±1.0	10.6±1.1
mean	20.1±0.2	20.2±0.1	5.7±0.9	10.2±0.9

Table B.3.: Effiencies of both cells measured after each manipulation. The efficiencies measured after each step are calculated from the average of at least four J-V curves

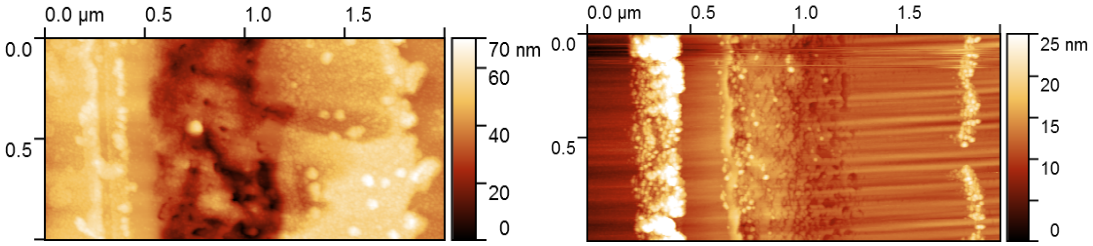

Figure B.11.: Cross sections of the two investigated PSC architectures (left planar, right mesoporous). The planar cross section was prepared with the Hitachi device, the shown meso cross section with the FIB

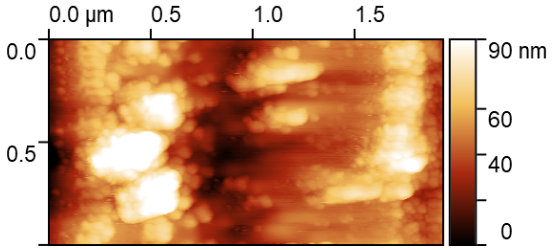

Figure B.12: Meso cell cross section polished with the Hitachi device. Artifacts are visible that originate from a 'double tip'. The double tip leads to a lateral resolution loss in the direction the artifacts appear (horizontal).

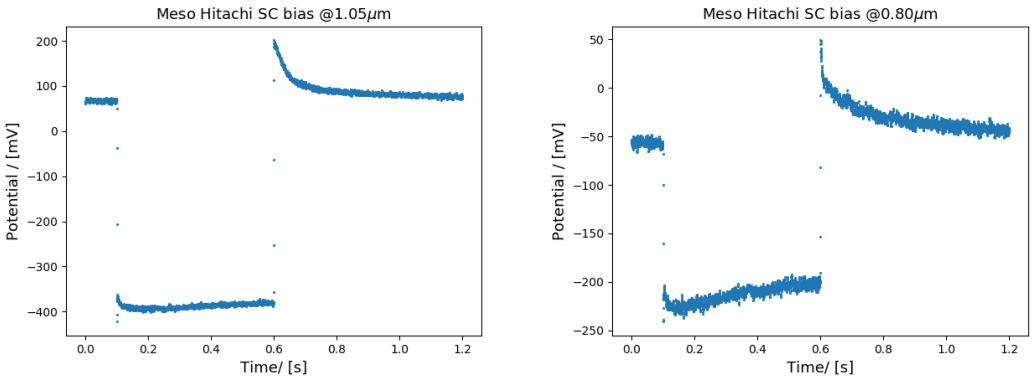

Figure B.13.: Potential dynamics in the bulk perovskite layer of the mesoporous cell. The left graph is from a region near the P-M interface, the right one from a region near the S-P interface. The graphs inbetween this 300nm region show the same features.

Bias On

Position	τ_1 / [ms]	τ_2 / [ms]
Spiro	8.7±0.4	784.4±259.5
S-P interface	14.5±0.5	571.9±68.1
Perovskite	x	x
P-M interface	x	x
Meso layer	x	x
FTO	0.3±0.3	-

Table B.4.: Results of the exponential fits to the relative mesoporous cell potential for the bias-on part. Where τ_2 is missing, we used single exponential fits (marked with -). The x represents locations where more than two processes can be identified. We cannot apply the model of a double exponential here.

Bias Off

Position	τ_1 / [ms]	τ_2 / [ms]
Spiro	5.7±0.3	f
S-P interface	1.1±0.3	329.7±14.4
Perovskite	21.1±0.3	166.6±2.7
P-M interface	4.3±1.7	55.0±0.3
Meso layer	1.3±0.8	53.3±0.4
FTO	1.0±0.3	-

Table B.5.: Results of the exponential fits to the bias-off part. Where τ_2 is missing, we used single exponential fits (marked with -). The f represents locations where our fitting program could not find optimal parameters.

References

[1] Stefan Weber, Ilka Maria Hermes, Silver Hamill Turren Cruz, Christopher Gort, Victor W Bergmann, Laurent Gilson, Anders Hagfeldt, Michael Grätzel, Wolfgang Tress, and Ruediger Berger.
How the formation of interfacial charge causes hysteresis in perovskite solar cells.
Energy & Environmental Science, 2018.

[2] K.-P. Schröder and Robert Connon Smith.
Distant future of the Sun and Earth revisited.
Monthly Notices of the Royal Astronomical Society, 386(1):155–163, 03 2008.

[3] Russell S Ohl.
Light-sensitive electric device, June 25 1946.
US Patent 2,402,662.

[4] Fraunhofer Institute for Solar energy.
Photovoltaics report, 2018.
`https://www.ise.fraunhofer.de/content/dam/ise/de/documents/publications/studies/Photovoltaics-Report.pdf` , [Online; accessed 26.02.2019].

[5] Victor W. Bergmann, Stefan A. L. Weber, F. Javier Ramos, Mohammad Khaja Nazeeruddin, Michael Grätzel, Dan Li, Anna L. Domanski, Ingo Lieberwirth, Shahzada Ahmad, and Rüdiger Berger.
Real-space observation of unbalanced charge distribution inside a perovskite-sensitized solar cell.
Nature Communications, 5:5001 EP –, Sep 2014.
Article.

[6] James R. Chelikowsky and Marvin L. Cohen.
Electronic structure of silicon.
Phys. Rev. B, 10:5095–5107, Dec 1974.

[7] Cepheiden.
Bandstruktur, Wikipedia, the free encyclopedia, 2018.
`https://de.wikipedia.org/wiki/Datei:Band_structure_Si_schematic.svg#file` , [Online; accessed 26.02.2019].

[8] R. Gross and A. Marx.
Festkörperphysik.
De Gruyter Studium. De Gruyter, 2014.

[9] Peter Würfel and Uli Würfel.

Physics of solar cells: from basic principles to advanced concepts.
John Wiley & Sons, 2016.

[10] Peter Sigmund.
Theory of sputtering. i. sputtering yield of amorphous and polycrystalline targets.
Phys. Rev., 184:383–416, Aug 1969.

[11] Peter Sigmund.
Elements of sputtering theory.
Nanofabrication by Ion-Beam Sputtering: Fundamentals and Applications, pages 1–40, 2012.

[12] Qiangmin Wei, Kun-Dar Li, Jie Lian, and Lumin Wang.
Angular dependence of sputtering yield of amorphous and polycrystalline materials.
Journal of Physics D: Applied Physics, 41(17):172002, 2008.

[13] Wolfgang Eckstein.
Sputtering Yields, pages 33–187.
Springer Berlin Heidelberg, Berlin, Heidelberg, 2007.

[14] Zurich Instruments.
White paper - principles of lock-in detection and the state of the art, 2016.
`https://www.zhinst.com/sites/default/files/li_primer/zi_whitepaper_principles_of_lock-in_detection.pdf` , [Online; accessed 26.02.2019].

[15] Akihiro Kojima, Kenjiro Teshima, Yasuo Shirai, and Tsutomu Miyasaka.
Organometal halide perovskites as visible-light sensitizers for photovoltaic cells.
Journal of the American Chemical Society, 131(17):6050–6051, 2009.

[16] Hui-Seon Kim, Chang-Ryul Lee, Jeong-Hyeok Im, Ki-Beom Lee, Thomas Moehl, Arianna Marchioro, Soo-Jin Moon, Robin Humphry-Baker, Jun-Ho Yum, Jacques E. Moser, Michael Grätzel, and Nam-Gyu Park.
Lead iodide perovskite sensitized all-solid-state submicron thin film mesoscopic solar cell with efficiency exceeding 9%.
Nature, 2(591), 2012.

[17] Nam-Gyu Park.
Organometal perovskite light absorbers toward a 20% efficiency low-cost solid-state mesoscopic solar cell.
The Journal of Physical Chemistry Letters, 4(15):2423–2429, 2013.

[18] Guichuan Xing, Nripan Mathews, Shuangyong Sun, Swee Sien Lim, Yeng Ming Lam, Michael Grätzel, Subodh Mhaisalkar, and Tze Chien Sum.
Long-range balanced electron- and hole-transport lengths in organic-inorganic CH3NH3PbI3.
Science, 342(6156):344–347, 2013.

[19] Samuel D Stranks, Giles E Eperon, Giulia Grancini, Christopher Menelaou,

Marcelo JP Alcocer, Tomas Leijtens, Laura M Herz, Annamaria Petrozza, and Henry J Snaith.
Electron-hole diffusion lengths exceeding 1 micrometer in an organometal trihalide perovskite absorber.
Science, 342(6156):341–344, 2013.

[20] T. Umebayashi, K. Asai, T. Kondo, and A. Nakao.
Electronic structures of lead iodide based low-dimensional crystals.
Phys. Rev. B, 67:155405, Apr 2003.

[21] William Shockley and Hans J. Queisser.
Detailed balance limit of efficiency of p-n junction solar cells.
Journal of Applied Physics, 32(3):510–519, 1961.

[22] Jongseob Kim, Sung-Hoon Lee, Jung Hoon Lee, and Ki-Ha Hong.
The role of intrinsic defects in methylammonium lead iodide perovskite.
The journal of physical chemistry letters, 5(8):1312–1317, 2014.

[23] Wan-Jian Yin, Tingting Shi, and Yanfa Yan.
Unusual defect physics in CH3NH3PbI3 perovskite solar cell absorber.
Applied Physics Letters, 104(6):063903, 2014.

[24] Julian Burschka, Norman Pellet, Soo-Jin Moon, Robin Humphry-Baker, Peng Gao, Mohammad K. Nazeeruddin, and Michael Grätzel.
Sequential deposition as a route to high-performance perovskite-sensitized solar cells.
Nature, 499(316), 2013.

[25] Tomas Leijtens, Giles E. Eperon, Sandeep Pathak, Antonio Abate, Michael M. Lee, and Henry J. Snaith.
Overcoming ultraviolet light instability of sensitized TiO2 with meso-superstructured organometal tri-halide perovskite solar cells.
Nature Communications, 4:2885, 2013.

[26] Guangda Niu, Wenzhe Li, Fanqi Meng, Liduo Wang, Haopeng Dong, and Yong Qiu.
Study on the stability of CH3NH3PbI3 films and the effect of post-modification by aluminum oxide in all-solid-state hybrid solar cells.
J. Mater. Chem. A, 2:705–710, 2014.

[27] Zhaoning Song, Chad L. McElvany, Adam B. Phillips, Ilke Celik, Patrick W. Krantz, Suneth C. Watthage, Defne Liyanage, Geethika K.and Apul, and Michael J. Heben.
A technoeconomic analysis of perovskite solar module manufacturing with low-cost materials and techniques.
Energy Environ. Sci., 10:1297–1305, 2017.

[28] Tomas Leijtens, Rohit Prasanna, Kevin A Bush, Giles E Eperon, James A Raiford, Aryeh Gold-Parker, Eli J Wolf, Simon A Swifter, Caleb C Boyd, Hsin-Ping Wang, et al.

Tin–lead halide perovskites with improved thermal and air stability for efficient all-perovskite tandem solar cells.
Sustainable Energy & Fuels, 2(11):2450–2459, 2018.

[29] Weijun Ke, Constantinos C. Stoumpos, and Mercouri G. Kanatzidis.
"Unleaded" perovskites: Status quo and future prospects of tin-based perovskite solar cells.
Advanced Materials, 0(0):1803230.

[30] Emilio J Juarez-Perez, Rafael S Sanchez, Laura Badia, Germá Garcia-Belmonte, Yong Soo Kang, Ivan Mora-Sero, and Juan Bisquert.
Photoinduced giant dielectric constant in lead halide perovskite solar cells.
The journal of physical chemistry letters, 5(13):2390–2394, 2014.

[31] Christopher Eames, Jarvist M Frost, Piers RF Barnes, Brian C O'regan, Aron Walsh, and M Saiful Islam.
Ionic transport in hybrid lead iodide perovskite solar cells.
Nature communications, 6:7497, 2015.

[32] Henry J. Snaith, Antonio Abate, James M. Ball, Giles E. Eperon, Tomas Leijtens, Nakita K. Noel, Samuel D. Stranks, Jacob Tse-Wei Wang, Konrad Wojciechowski, and Wei Zhang.
Anomalous hysteresis in perovskite solar cells.
The Journal of Physical Chemistry Letters, 5(9):1511–1515, 2014.

[33] Martin A Green, Anita Ho-Baillie, and Henry J Snaith.
The emergence of perovskite solar cells.
Nature photonics, 8(7):506, 2014.

[34] Jun Hong Noh, Sang Hyuk Im, Jin Hyuck Heo, Tarak N Mandal, and Sang Il Seok.
Chemical management for colorful, efficient, and stable inorganic–organic hybrid nanostructured solar cells.
Nano letters, 13(4):1764–1769, 2013.

[35] Giles E Eperon, Samuel D Stranks, Christopher Menelaou, Michael B Johnston, Laura M Herz, and Henry J Snaith.
Formamidinium lead trihalide: a broadly tunable perovskite for efficient planar heterojunction solar cells.
Energy & Environmental Science, 7(3):982–988, 2014.

[36] Teck Ming Koh, Kunwu Fu, Yanan Fang, Shi Chen, T. C. Sum, Nripan Mathews, Subodh G. Mhaisalkar, Pablo P. Boix, and Tom Baikie.
Formamidinium-containing metal-halide: An alternative material for near-ir absorption perovskite solar cells.
The Journal of Physical Chemistry C, 118(30):16458–16462, 2014.

[37] Hyosung Choi, Jaeki Jeong, Hak-Beom Kim, Seongbeom Kim, Bright Walker, Gi-Hwan Kim, and Jin Young Kim.

Cesium-doped methylammonium lead iodide perovskite light absorber for hybrid solar cells.
Nano Energy, 7:80 – 85, 2014.

[38] Michael Saliba, Taisuke Matsui, Ji-Youn Seo, Konrad Domanski, Juan-Pablo Correa-Baena, Mohammad Khaja Nazeeruddin, Shaik M Zakeeruddin, Wolfgang Tress, Antonio Abate, Anders Hagfeldt, et al.
Cesium-containing triple cation perovskite solar cells: improved stability, reproducibility and high efficiency.
Energy & environmental science, 9(6):1989–1997, 2016.

[39] Jon M Azpiroz, Edoardo Mosconi, Juan Bisquert, and Filippo De Angelis.
Defect migration in methylammonium lead iodide and its role in perovskite solar cell operation.
Energy & Environmental Science, 8(7):2118–2127, 2015.

[40] Wolfgang Tress.
Metal halide perovskites as mixed electronic–ionic conductors: Challenges and opportunities—from hysteresis to memristivity.
The journal of physical chemistry letters, 8(13):3106–3114, 2017.

[41] Hui-Seon Kim and Nam-Gyu Park.
Parameters affecting i–v hysteresis of ch3nh3pbi3 perovskite solar cells: effects of perovskite crystal size and mesoporous tio2 layer.
The journal of physical chemistry letters, 5(17):2927–2934, 2014.

[42] Giselle A. Elbaz, Daniel B. Straus, Octavi E. Semonin, Trevor D. Hull, Daniel W. Paley, Philip Kim, Jonathan S. Owen, Cherie R. Kagan, and Xavier Roy.
Unbalanced hole and electron diffusion in lead bromide perovskites.
Nano Letters, 17(3):1727–1732, 2017.

[43] Rafael S Sanchez, Victoria Gonzalez-Pedro, Jin-Wook Lee, Nam-Gyu Park, Yong Soo Kang, Ivan Mora-Sero, and Juan Bisquert.
Slow dynamic processes in lead halide perovskite solar cells. characteristic times and hysteresis.
The journal of physical chemistry letters, 5(13):2357–2363, 2014.

[44] Jing Wei, Yicheng Zhao, Heng Li, Guobao Li, Jinlong Pan, Dongsheng Xu, Qing Zhao, and Dapeng Yu.
Hysteresis analysis based on the ferroelectric effect in hybrid perovskite solar cells.
The journal of physical chemistry letters, 5(21):3937–3945, 2014.

[45] Wolfgang Tress, Nevena Marinova, Thomas Moehl, Shaik Mohammad Zakeeruddin, Mohammad Khaja Nazeeruddin, and Michael Grätzel.
Understanding the rate-dependent j–v hysteresis, slow time component, and aging in ch 3 nh 3 pbi 3 perovskite solar cells: the role of a compensated electric field.
Energy & Environmental Science, 8(3):995–1004, 2015.

[46] Daniel A Jacobs, Yiliang Wu, Heping Shen, Chog Barugkin, Fiona J Beck, Thomas P White, Klaus Weber, and Kylie R Catchpole.
Hysteresis phenomena in perovskite solar cells: the many and varied effects of ionic accumulation.
Physical Chemistry Chemical Physics, 19(4):3094–3103, 2017.

[47] EL Unger, ET Hoke, CD Bailie, WH Nguyen, AR Bowring, T Heumüller, MG Christoforo, and MD McGehee.
Hysteresis and transient behavior in current–voltage measurements of hybrid-perovskite absorber solar cells.
Energy & Environmental Science, 7(11):3690–3698, 2014.

[48] Heetae Yoon, Seong Min Kang, Jong-Kwon Lee, and Mansoo Choi.
Hysteresis-free low-temperature-processed planar perovskite solar cells with 19.1% efficiency.
Energy & Environmental Science, 9(7):2262–2266, 2016.

[49] Yi Hou, Cesar Omar Ramirez Quiroz, Simon Scheiner, Wei Chen, Tobias Stubhan, Andreas Hirsch, Marcus Halik, and Christoph J. Brabec.
Low-temperature and hysteresis-free electron-transporting layers for efficient, regular, and planar structure perovskite solar cells.
Advanced Energy Materials, 5(20):1501056, 2015.

[50] G. Binnig, C. F. Quate, and Ch. Gerber.
Atomic force microscope.
Phys. Rev. Lett., 56:930–933, Mar 1986.

[51] Franz J. Giessibl.
Atomic resolution of the silicon (111)-(7x7) surface by atomic force microscopy.
Science, 267(5194):68–71, 1995.

[52] M. J. Higgins, R. Proksch, J. E. Sader, M. Polcik, S. Mc Endoo, J. P. Cleveland, and S. P. Jarvis.
Noninvasive determination of optical lever sensitivity in atomic force microscopy.
Review of Scientific Instruments, 77(1):013701, 2006.

[53] Phil Attard, Torbjörn Pettersson, and Mark W. Rutland.
Thermal calibration of photodiode sensitivity for atomic force microscopy.
Review of Scientific Instruments, 77(11):116110, 2006.

[54] Adam Foster and Werner A Hofer.
Scanning probe microscopy: atomic scale engineering by forces and currents.
Springer Science & Business Media, 2006.

[55] Hans-Jürgen Butt, Brunero Cappella, and Michael Kappl.
Force measurements with the atomic force microscope: Technique, interpretation and applications.
Surface science reports, 59(1-6):1–152, 2005.

[56] E. Meyer, H.J. Hug, and R. Bennewitz.
Scanning Probe Microscopy: The Lab on a Tip.

Advanced Texts in Physics. Springer Berlin Heidelberg, 2013.

[57] Johannes Diderik Van der Waals.
Over de Continuiteit van den Gas-en Vloeistoftoestand, volume 1.
Sijthoff, 1873.

[58] Igor Ekhiel'evich Dzyaloshinskii, EM Lifshitz, Lev P Pitaevskii, MG Priestley, et al.
The general theory of van der waals forces.
In *Perspectives in Theoretical Physics*, pages 443–492. Elsevier, 1992.

[59] Y. Martin, C. C. Williams, and H. K. Wickramasinghe.
Atomic force microscope–force mapping and profiling on a sub 100-å scale.
Journal of Applied Physics, 61(10):4723–4729, 1987.

[60] T. R. Albrecht, P. Grütter, D. Horne, and D. Rugar.
Frequency modulation detection using high-q cantilevers for enhanced force microscope sensitivity.
Journal of Applied Physics, 69(2):668–673, 1991.

[61] Takeshi Fukuma, Jason I. Kilpatrick, and Suzanne P. Jarvis.
Phase modulation atomic force microscope with true atomic resolution.
Review of Scientific Instruments, 77(12):123703, 2006.

[62] Ricardo García and Rubén Pérez.
Dynamic atomic force microscopy methods.
Surface Science Reports, 47(6):197 – 301, 2002.

[63] Franz J. Giessibl.
Forces and frequency shifts in atomic-resolution dynamic-force microscopy.
Phys. Rev. B, 56:16010–16015, Dec 1997.

[64] Ulrich Zerweck, Christian Loppacher, Tobias Otto, Stefan Grafström, and Lukas M. Eng.
Accuracy and resolution limits of kelvin probe force microscopy.
Phys. Rev. B, 71:125424, Mar 2005.

[65] Amelie Axt, Ilka M. Hermes, Victor W. Bergmann, Niklas Tausendpfund, and Stefan A. L. Weber.
Know your full potential: Quantitative kelvin probe force microscopy on nanoscale electrical devices.
Beilstein Journal of Nanotechnology, 9:1809–1819, 2018.

[66] S. A. Burke, J. M. LeDue, Y. Miyahara, J. M. Topple, S. Fostner, and P. Grütter.
Determination of the local contact potential difference of ptcda on nacl: a comparison of techniques.
Nanotechnology, 20(26):264012, 2009.

[67] Ch Sommerhalter, Th Glatzel, Th.W Matthes, A Jäger-Waldau, and M.Ch Lux-Steiner.
Kelvin probe force microscopy in ultra high vacuum using amplitude modulation detection of the electrostatic forces.

Applied Surface Science, 157(4):263–268, 2000.

[68] Shin'ichi Kitamura, Katsuyuki Suzuki, Masashi Iwatsuki, and C.B Mooney.
Atomic-scale variations in contact potential difference on au/si(111) 7x7 surface in ultrahigh vacuum.
Applied Surface Science, 157(4):222 – 227, 2000.

[69] Joseph L Garrett and Jeremy N Munday.
Fast, high-resolution surface potential measurements in air with heterodyne kelvin probe force microscopy.
Nanotechnology, 27(24):245705, 2016.

[70] Liam Collins, Alex Belianinov, Suhas Somnath, Brian J Rodriguez, Nina Balke, Sergei V Kalinin, and Stephen Jesse.
Multifrequency spectrum analysis using fully digital g mode-kelvin probe force microscopy.
Nanotechnology, 27(10):105706, 2016.

[71] Liam Collins, Mahshid Ahmadi, Ting Wu, Bin Hu, Sergei V. Kalinin, and Stephen Jesse.
Breaking the time barrier in kelvin probe force microscopy: Fast free force reconstruction using the g-mode platform.
ACS Nano, 11(9):8717–8729, 2017.
PMID: 28780850.

[72] Mathias Uller Rothmann, Wei Li, Ye Zhu, Amelia Liu, Zhiliang Ku, Udo Bach, Joanne Etheridge, and Yi-Bing Cheng.
Structural and chemical changes to CH3NH3PbI3 induced by electron and gallium ion beams.
Advanced Materials, 30(25):1800629.

[73] Ilka M. Hermes, Yi Hou, Victor W. Bergmann, Christoph J. Brabec, and Stefan A. L. Weber.
The interplay of contact layers: How the electron transport layer influences interfacial recombination and hole extraction in perovskite solar cells.
The Journal of Physical Chemistry Letters, 9(21):6249–6256, 2018.
PMID: 30256640.

[74] Aleksandra Wypych, Izabela Bobowska, Milena Tracz, Agnieszka Opasinska, Slawomir Kadlubowski, Alicja Krzywania-Kaliszewska, Jaroslaw Grobelny, and Piotr Wojciechowski.
Dielectric properties and characterisation of titanium dioxide obtained by different chemistry methods.
Journal of Nanomaterials, 2014, 2014.

[75] K Bruce Winterbon, Peter Sigmund, and JB Sanders.
Spatial distribution of energy deposited by atomic particles in elastic collisions.
Kgl. Dan. Vidensk. Selsk., Mat.-Fys. Medd. 37: 14-(1970)., 1970.

[76] Durmus U. Karatay, Jeffrey S. Harrison, Micah S. Glaz, Rajiv Giridharagopal, and David S. Ginger.
Fast time-resolved electrostatic force microscopy: Achieving sub-cycle time resolution.
Review of Scientific Instruments, 87(5):053702, 2016.

[77] Yves Martin, David W. Abraham, and H. Kumar Wickramasinghe.
High-resolution capacitance measurement and potentiometry by force microscopy.
Applied Physics Letters, 52(13):1103–1105, 1988.

[78] Rajiv Giridharagopal, Glennis E. Rayermann, Guozheng Shao, David T. Moore, Obadiah G. Reid, Andreas F. Tillack, David. J. Masiello, and David S. Ginger.
Submicrosecond time resolution atomic force microscopy for probing nanoscale dynamics.
Nano Letters, 12(2):893–898, 2012.
PMID: 22248070.

[79] Samuel D Stranks and Henry J Snaith.
Metal-halide perovskites for photovoltaic and light-emitting devices.
Nature nanotechnology, 10(5):391, 2015.

[80] Jeffrey A. Christians, Severin N. Habisreutinger, Joseph J. Berry, and Joseph M. Luther.
Stability in perovskite photovoltaics: A paradigm for newfangled technologies.
ACS Energy Letters, 3(9):2136–2143, 2018.

[81] Stephan van Reenen, Martijn Kemerink, and Henry J. Snaith.
Modeling anomalous hysteresis in perovskite solar cells.
The Journal of Physical Chemistry Letters, 6(19):3808–3814, 2015.
PMID: 26722875.

[82] J Beilsten-Edmands, GE Eperon, RD Johnson, HJ Snaith, and PG Radaelli.
Non-ferroelectric nature of the conductance hysteresis in CH3NH3PbI3 perovskite-based photovoltaic devices.
Applied Physics Letters, 106(17):173502, 2015.

[83] Philip Calado, Andrew M Telford, Daniel Bryant, Xiaoe Li, Jenny Nelson, Brian C O'Regan, and Piers RF Barnes.
Evidence for ion migration in hybrid perovskite solar cells with minimal hysteresis.
Nature communications, 7:13831, 2016.

[84] Marina R Filip, Giles E Eperon, Henry J Snaith, and Feliciano Giustino.
Steric engineering of metal-halide perovskites with tunable optical band gaps.
Nature communications, 5:5757, 2014.

[85] Sascha Sadewasser and Thilo Glatzel.
Kelvin probe force microscopy, volume 8.
Springer.

[86] H.J. Butt and M. Kappl.
Surface and Interfacial Forces.
Wiley, 2018.

[87] D. M. Chapin, C. S. Fuller, and G. L. Pearson.
A new silicon p-n junction photocell for converting solar radiation into electrical power.
Journal of Applied Physics, 25(5):676–677, 1954.

Acknowledgements

In the following I want to thank the people that helped me through this work an without whom this thesis could not have been accomplished the way it was.

I want to thank Prof. Stefan Weber who could not have been a better mentor. He always was open for advice and going in and out of his office always gave me insights. To cite a metaphor by Bernhard von Chartres, I truly stood on the shoulders of a giant.
Ilka Hermes who not lesser helped in my struggles at the MPI-P and who is the coolest gurl there is. Go on be a professor, I dare you.
I want to thank Prof. Hans-Joachim Elmers for kindly agreeing to take his time to be the second referee for this thesis.

A shout out goes to all the Weberknechts including Knecht of honour Alex Klasen. I am sad to soon leave this house of madness that helped to keep a clear head. Special thanks to Amy Random Stetten, who helped with my english skills. Dank je David van Duinen for your cool get togethers and your Stroopwaffels.
I want to thank everyone else at the MPI-P who gave me a academic home.

A great thank you to all my friends. I hope we will have our table of regulars until we get old.

Most important I want to thank my family especially my mother for supporting me in every way she can. I am deeply thankful for that.